Phosphate Boosts Nonhydroxyl Radical Species Production upon Air Oxidation of Magnetite and Iron Sulfides at Neutral pH

Guillaume Morin, Frédéric Averseng, Xavier Carrier, Pierre Le Pape, Yishan Du, Yusheng Honge, Elora Bourbon, Giuseppe Sportelli, Tiago A da Silva, Alberto Mezzetti, et al.

Phosphate Boosts Non-Hydroxyl Radical Species Production upon Air-Oxidation of Magnetite and Iron Sulfides at Neutral pH

Guillaume Morin[1*], Frédéric Averseng[2], Xavier Carrier[2], Pierre Le Pape[1], Yishan Du[1], Yusheng HongE[1], Elora Bourbon[1], Giuseppe Sportelli[2,1], Tiago A. Da Silva[1,2], Alberto Mezzetti[2], Camille Baya[1], Thierry Allard[1], Jessica Brest[1], Maryse Rouelle[3]

[1]Institut de Minéralogie, de Physique des Matériaux et de Cosmochimie (IMPMC)
UMR 7590, CNRS-Sorbonne Université – MNHN – IRD, 4 place Jussieu, 75252 Paris Cedex 05, France

[2]Laboratoire de Réactivité de Surface (LRS)
UMR 7197, Sorbonne Université – CNRS, 4 place Jussieu, 75252 Paris Cedex 05, France

[3]Milieux Environnementaux, Transferts et Interactions dans les hydrosystèmes et les Sols (METIS), UMR 7619, Sorbonne Université – CNRS – EPHE, 4 place Jussieu, 75252 Paris Cedex 05, France.

Pre-proof revised version #2 April 26, 2023 published in *The Journal of Physical Chemistry C*

*Corresponding author: guillaume.morin@sorbonne-universite.fr

Abstract

Heterogeneous Fenton-like reactions using O_2 as sole oxidant are gaining interest for designing organic contaminant degradation in soils and groundwaters, since they may provide alternatives to current processes involving strong oxidants. Indeed, several Fe(II)-bearing oxide and sulfide mineral phases have been proven to generate reactive species upon air-oxidation. However, the mechanisms of these reactions and the identity of reactive species produced upon oxygenation may deserve further research. Here, we show using Electron Paramagnetic Resonance (EPR) spectroscopy combined with the 5,5-Dimethyl-1-pyrroline N-oxide (DMPO) spin-trap, that air oxidation of pH7 phosphate buffered aqueous suspensions of magnetite (Fe_3O_4) or mackinawite (FeS) nanoparticles produces a reactive species that is distinct from the hydroxyl radical (•OH) and abstracts a hydrogen atom from ethanol. This reactive species grows dramatically with phosphate concentration, and ultra-filtration reveals that it occurs as both aqueous and surface species. Based on these evidences and from extant reports, we hypothesize that the non-hydroxyl reactive species produced is Fe(IV), whose formation is enhanced in the presence of phosphate ligands. Fe_3O_4 magnetite (~14 nm) generates about 30% more of this putative ferryl species than FeS mackinawite (~9 nm), while FeS_2 (pyrite ~12 nm + marcasite ~4 nm) appears unreactive under these conditions.

Keywords: Reactive oxygen species, phosphate, hydroxyl radical, ferryl ion, magnetite, mackinawite, pyrite, Fenton, ROS, DMPO, EPR, XAS, Fe(IV)

Synopsis: Sole air-oxidation of Fe_3O_4 or FeS at pH 7 does not significantly produce the hydroxyl radical but another species favored by phosphate ligand and able to oxidize ethanol, likely Fe(IV).

Introduction

A growing interest has risen to use air-oxidation of iron minerals as a source for reactive species, especially in order to progress in decreasing the environmental impacts of oxidative pollutant degradation processes, particularly by limiting or avoiding the use of strong oxidants. For instance, several organic contaminants can be degraded upon air-oxidation of nanoparticulate zero-valent iron (nZVI)[1], fine-particle Fe_3O_4 (magnetite)[2,3], FeS[4] and clay minerals[5]. These degradation reactions are thought to proceed via to reactive species generated through oxidation of the Fe(II)-substrate by airborne O_2, these reactive species being then able to oxidize certain organic molecules[1]. However, especially concerning air-oxidation of iron substrates, the identity of the involved reactive species is still debated. In particular, the respective roles of the hydroxyl radical[2-6] and the ferryl ion (i.e., Fe(IV) in the form of FeO^{2+})[7-10] are particularly difficult to distinguish. Nevertheless, various studies using measurements of the conversion rate of benzoic acid (BA) into *para*-hydoxybenzoic acid (*p*-HBA) have proven the ability of zero-valent iron[7], FeS[4,11], clay-minerals[6] as well as natural sediments[12] to produce reactive species upon oxygenation. However, the relative efficiencies of such iron substrates have rarely been evaluated within a same study under equivalent conditions.

In the present study, we aimed at contributing to this active research field by directly comparing the ability of environmentally relevant minerals, i.e., fine particle Fe_3O_4 (magnetite), FeS (mackinawite) and FeS_2 (pyrite/marcasite) to produce reactive species upon airborne O_2-oxidation on a same basis. We chose to use Electron Paramagnetic Resonance (EPR) spin-trapping to evaluate the rate of paramagnetic adduct production upon oxidation of the iron substrates in order to provide a complementary approach to, for instance, the BA/*p*-HBA conversion rate measurements that have already been developed in the literature. Although EPR spin-trapping has been also previously used in the context of air-oxidation of Fe-substrates for fingerprinting reactive species, especially the hydroxyl radical (•OH)[2,4,11], our approach here aimed at tentatively use this method to compare the reactivity of various iron substrates on a quantitative basis. The obtained results yield straightforward information on the relative efficiency of these three substrates to produce reactive species upon short-term oxidation, i.e. within the 1-20 min range. The identity of these reactive species is discussed by comparing air- and H_2O_2-oxidation experiments conducted in the presence or absence of ethanol as radical scavenger and as a function of phosphate buffer concentration.

Experimental Methods

Syntheses procedures and mineralogical analyses. All syntheses and sample preparation procedures were performed in a Jacomex™ glove box under N_2 atmosphere (<5 ppm O_2). All solutions were prepared in the glove box with O_2-free milli-Q water, i.e. degassed under N_2-bubbling for 40 min at 75°C.

Fe_3O_4 (magnetite) was synthesized according to a proven procedure[3,13] by coprecipitating Fe^{2+} and Fe^{3+} at a final pH of 12. Briefly, acidic stock solutions of 1M $FeCl_3$•$6H_2O$ and 1M $FeCl_2$•$4H_2O$ were mixed in

stoichiometric proportions (2:1) and neutralized to pH 12 by adding appropriate volume of 1M NaOH. The suspension was sealed with butyl rubber stopper, agitated for 24 h at 25°C, three times centrifuged at 6000 rpm for 20 min and washed with O_2-free milli-Q water, and vacuum-dried in a dessicator in the glove box.

FeS (mackinawite) was synthesized by reacting Fe^{2+} with aqueous H_2S followed by aging[14,15]. Briefly, a stock solution of 0.625M $FeCl_2$•$4H_2O$ was mixed in equal proportions with a 0.625M Na_2S solution and was then 7-fold diluted in O_2-free milli-Q water. The suspension was sealed with butyl rubber stopper, agitated for 65 h at 25°C, aged for 11 months, centrifuged at 6000 rpm for 20 min and washed three times with O_2-free milli-Q water, and vacuum-dried in a dessicator in the glove box.

FeS_2 (65% pyrite – 34% nanomarcassite - 1% α-sulfur) was synthesized by reacting Fe^{3+} with aqueous H_2S[14-16]. A stock solution of 0.625M $FeCl_3$•$6H_2O$ was mixed in equal proportions with a 0.625M Na_2S solution and then 4-fold diluted in O_2-free milli-Q water. The suspension was sealed with butyl rubber stopper, agitated for 528 h at 25°C, aged for 19 months, centrifuged at 6000 rpm for 20 min and washed three times with O_2-free milli-Q water, and vacuum-dried in a dessicator in the glove box.

The mineralogical composition of each substrate was checked by using Rietveld analysis of powder X-ray Diffraction patterns collected under anoxic conditions. For this purpose, a thin coating of powder was deposited on a pure silicon-wafer - zero-background - sample-holder that was mounted within an anoxic chamber (IMPMC) equipped with a Kapton window. XRD data were collected in Bragg-Brentano geometry using an X'pert pro® Panalytical™ diffractometer equipped with an X'celerator® solid state detector, counting 4h per sample in continuous mode over the 5-80° 2θ-range with a 0.0334° 2θ-step.

Rietveld analysis of XRD patterns collected on the synthetic samples (Figure S1; Table S1) indicated that the magnetite and mackinawite samples were mineralogically pure except for traces of NaCl in the magnetite sample, whereas the pyrite (cubic FeS_2) sample contained 34 wt% of nanosized (4 nm) marcasite (orthorhombic FeS_2) and 1 wt% of elemental sulfur. The average MCD sizes of magnetite (~14 nm), mackinawite (~9 nm) and pyrite (~12 nm) were of similar order of magnitude, and were consistent with Brunauer-Emmet-Teller (BET) surface areas determined as 103 and 122 m^2/g for magnetite and mackinawite, respectively. BET measurements could not be performed on our pyrite sample because of insufficient amount of material.

Oxidation experiments. Prior to oxidation experiments, mineral suspensions were prepared in the anoxic glove box by suspending a given weight of mineral powder in a solution consisting of 350 µL of 0.1M or 1M phosphate-buffer (pH 7, prepared from anhydrous NaH_2PO_4 and Na_2HPO_4), with or without addition of 16µL of 99%vol CH_3CH_2OH (ethanol), the mixture being then equilibrated overnight within a 5 mL glass vial closed by a butyl rubber stopper. A volume of 300 µL of 92 mM solution of the spin-trap 5,5-Dimethyl-1-pyrroline N-oxide (DMPO ≥ 98.0 % for ESR spectroscopy, Sigma Aldrich® #92688) was then added to the suspension in each vial within the glove box. The vials were then sealed with butyl rubber stoppers and taken out from the glove box for performing the oxidation experiments. Molarity of phosphate, ethanol and DMPO in the reaction vessel were thus 0.053 or 0.525 M, 0.407 M and 41 mM. Ethanol was used as additional radical trap ion order to decipher among possible reactive species, as discussed in the text.

Air-oxidation experiments were conducted by bubbling 100 mL air for 1 min into the mineral suspension followed by 1 min shaking. Air was bubbled using a 50 mL syringe with a needle plunging into the suspension, whereas another free needle ensured evacuation of the headspace overpressure. Immediately after air bubbling, the vials were shaken for 1 min before the suspension was sampled using a 5mL syringe and needle and readily filtered through a 0.2µm nylon filter. The filtrate was rapidly transferred into the Electron Paramagnetic Resonance (EPR) liquid flat-cell for measurements. The first EPR spectrum could be collected about 5 min after the beginning of the air bubbling that was taken as starting time (t = 0 min). The EPR spectrum of the filled liquid flat-cell was then monitored for one hour, collecting an EPR spectrum every five minutes. In order to maximize the radical species yield, complementary 20 min air-oxidation experiments were also performed following the same procedure, but using a gas ramp providing a flow rate of approximately 100 mL/min. Besides, to investigate the role of the dissolved species in free-radical production, complementary 1 min air-oxidation experiments were performed on the filtrate of the mineral suspension instead of the full suspension. Duplicate experiments were performed after having filtrated the anoxic mineral suspension through a 0.2µm nylon filter in the glove box, and single experiments were performed after 3kDa ultrafiltration also in the glove box.

Filtrates were analyzed after oxidation reactions to determine total dissolved Fe concentration. Aliquots of 200 µL were acidified using 69% NORMAPUR® nitric acid addition and appropriately diluted before being analyzed by inductively-coupled plasma-optical emission spectrometry (ICP-OES) (AGILENT 5100 SVDV) at the ALIPP6 platform of Sorbonne University. Uncertainties were ±2% as measured on standard reference samples.

Hydrogen peroxide (H_2O_2)-oxidation experiments were also carried out for a 12 mg magnetite suspension. For this purpose, the oxidation was performed by adding 50 µL of a 0.1M H_2O_2 solution and shaking for 2 min before sampling, filtrating and EPR monitoring, H_2O_2-spiking being taken as starting time.

For every above-mentioned experiment, suspensions were prepared with 12 mg of magnetite, or 4.6 mg of mackinawite, or 6.2 mg of pyrite. Assuming stoichiometric compositions for our mineral samples, these suspensions had a mineral concentration equivalent to a same total Fe(II) molarity of 78 mM. A blank experiment was also conducted without any solid. The 1 min air-oxidation experiments for magnetite and mackinawite were conducted in triplicate. Single experiments were conducted for pyrite because of low amount of available material.

Electron Paramagnetic Resonance (EPR) data collection and analysis. EPR spectra were collected at room temperature on the filtered solutions inserted in a 150 µL Suprasil® flat cell (JEOL ES-LC12: 10 x 0.3 x 50 mm^3 inner dimensions) using a JEOL FA-300 spectrometer operating at 9.4 GHz (X-band). All spectra were recorded using the same setup of EPR parameters. Microwave power, frequency modulation, amplitude modulation, time constant, and gain were 2 mW, 100kHz, 5 10^{-5} Tesla, 30 ms, 800, respectively, resulting in ~2 min long scans of 4096 points over the 0.33204 – 0.34204 Tesla (i.e., 3320.4 – 3420.4 Gauss) magnetic-field range. The magnetic-field offset related to the off-center position of the Hall-probe with respect to the

EPR cavity was corrected to -13.7 10^{-4} Tesla, as determined by setting the *g* value of the Bruker® strong-pitch standard to 2.0018.

For each oxidation experiment, a series of EPR spectra was collected on the filtered suspension every ~5 min during ~1 hour after the starting time corresponding to the beginning of air-bubbling in the mineral suspension. These time course measurements were designed to monitor the evolution of the EPR signal after a single 1min air-oxidation of the mineral suspension, as described in the above section. EPR spectra were least squares fit using the EPRPLP code[17] in order to extract EPR parameters of the observed free radical-DMPO adducts. This fitting procedure also yielded a scale factor proportional to the abundance of each adduct, which allowed us to monitor their evolution from sample to sample and over time. The scale factors values were converted to concentration units by comparison with the Bruker® strong-pitch EPR spectrum collected in the same conditions, equivalent to 0.11/0.0003 10^{13} = 3.67 10^{15} spin units per cm, which were then converted to molar concentrations of adducts in the flat-cell volume of 30µL per cm.

X-ray absorption spectroscopy data collection and analysis. X-ray absorption spectroscopy (XAS) analysis at the iron *K*-edge was performed on dried solid samples collected after similar air-oxidation protocol than that used for the EPR spin trapping experiments. The mineral suspensions contained 12, 4.3 and 6.2 mg of magnetite, mackinawite and pyrite, respectively, and were prepared with added DMPO, CH_3CH_2OH, and pH 7 phosphate buffer. After 1 min air bubbling, 1 min shaking and needle/syringe sampling, the suspensions were centrifuged for 1 min at 6000 rpm and immediately transferred into the anoxic glove box, in which they were vacuum dried in a dessicator. Pressed pellets were prepared by mixing appropriate amounts of the initial or oxidized mineral powders with cellulose. Data were collected at 10K in transmission detection mode at the SAMBA beamline of the SOLEIL synchrotron facility, Orsay (France), using a 220 double crystal monochromator with sagittal focusing of the second crystal and a liquid He cryostat. Energy was calibrated by setting to 9112 eV the first inflexion point of the absorption edge of a metallic iron foil collected in double-transmission setup. A series of 3 to 5 fast-scans of 5 min long was merged for each sample. XAS data were merged, normalized and background subtracted using the Athena software[18] to extract X-ray Absorption Near Edge Structure (XANES) and Extended X-ray Absorption Fine Structure (EXAFS) spectra. XANES and EXAFS data were analyzed using a least-squares Linear Combination Fitting (LCF) procedure, with a home-built software based on a Levenberg-Marquardt minimization algorithm[14-16,19].

Results and Discussion

Reactive species production after air-oxidation of magnetite, mackinawite or pyrite, with or without CH_3CH_2OH addition. Typical EPR spectra of the filtrates obtained after 1 min air-oxidation of the CH_3CH_2OH-added magnetite, mackinawite, pyrite and blank suspensions are displayed in Figure 1. The spectra in Figure 1a were collected on the filtrates at t = 25 min after the initial single 1 min long air-bubbling followed by 1 min shaking and immediate filtration. These spectra are largely dominated by that of an alkyl-

DMPO adduct interpreted as the α-hydroxyethyl radical, $CH_3CH•OH$-DMPO, with the following refined EPR parameters: g_{iso} =2.0054(1), A_{Hiso} = 0.00217(1) cm^{-1} [23.2(1) Gauss], A_{Niso} = 0.00150(1) cm^{-1} [16.0(1) Gauss] with a Gaussian line-shape and a full-width of 1.54(1) Gauss. These parameters are fully consistent with those of the $CH_3CH•OH$-DMPO adduct, as reported by Finkelstein[20] and Buettner[21]. In these air-oxidation experiments, a very minor contribution from a •OH-DMPO adduct could be added in the fit but did not exceed 1% of the most intense $CH_3CH•OH$-DMPO signal observed for magnetite, as illustrated in Figure S2. The slight asymmetry of the $CH_3CH•OH$-DMPO adduct signal results from two isomeric adducts with different C_2-H proton coupling constants[22] that are present in unequal proportions[23]. Such asymmetry due to the superposition of different conformers has been also reported for other adducts such as the superoxide-DMPO adduct, with obviously different hyperfine parameters[24]. In our case, a single component fit was found however accurate enough to quantify the $CH_3CH•OH$-DMPO adducts, as compared to a two-component fit (Figure S3; Table S3).

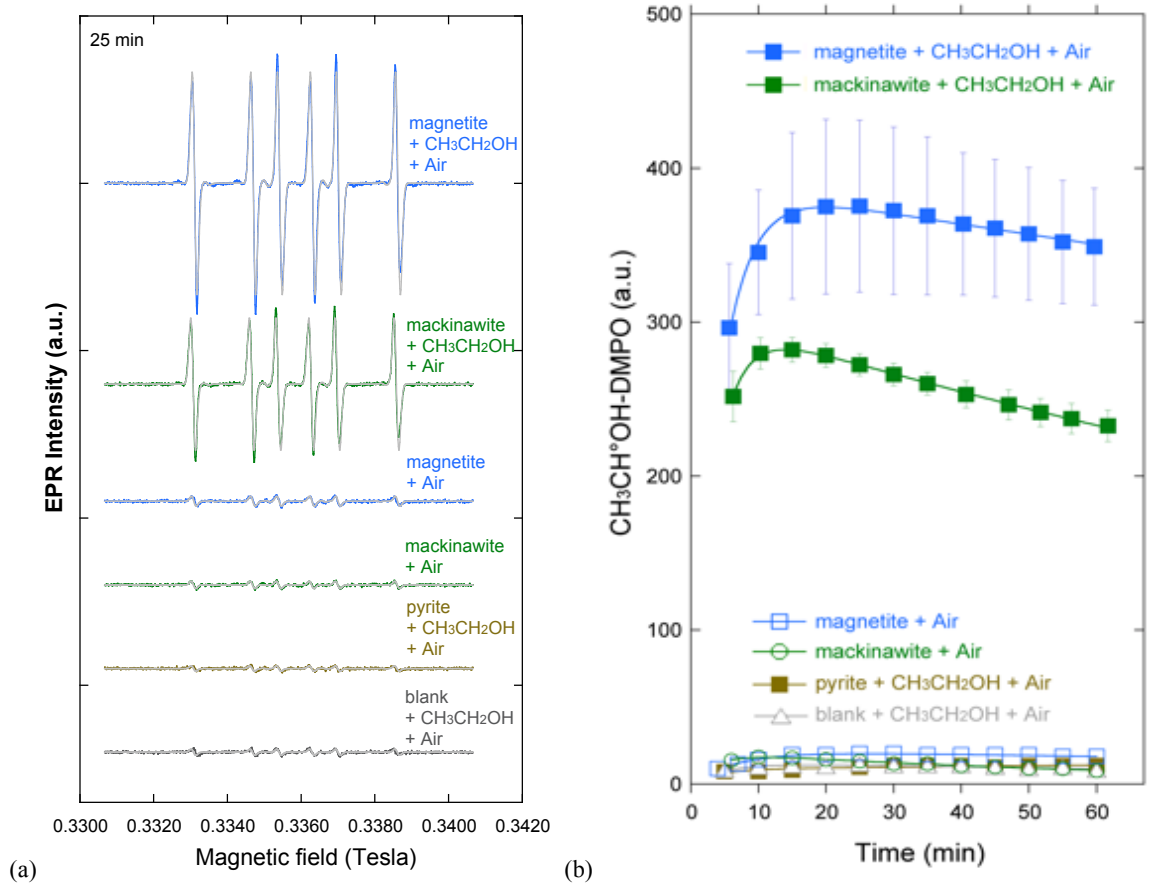

Figure 1. EPR monitoring of the DMPO-added mineral suspension (0.525 M phosphate buffer pH 7) after 1 min air-bubbling, 1 min shaking and immediate filtration. (a) EPR spectra taken 25 min after the start of 1 min air-bubbling of the magnetite (blue), mackinawite (green), pyrite (brown) and blank (gray) suspensions with prior addition of CH_3CH_2OH, and of the magnetite (blue) or mackinawite (green) experiments conducted with or without prior addition of CH_3CH_2OH. Fitting curves are displayed as light-gray lines, with fitting parameters reported in Table S2. (b) time-course evolution of the fitted $CH_3CH•OH$-DMPO adduct scale factor during 5 to 60 min EPR monitoring of the filtrates. Error bars correspond to the standard deviation on triplicate experiments for magnetite and mackinawite. The kinetics fit curves displayed as plain lines were obtained with Equation 1, with fitting parameters reported in Table 1.

For each substrate, similar shapes were observed for all EPR spectra as a function of time after the single 1 min air-oxidation but the intensity of the $CH_3CH•OH$-DMPO adduct signal significantly varied over the 60

min of EPR monitoring. These variations are displayed on Figure 1b, which represents the time-evolution of the scale factor value for the CH_3CH•OH-DMPO adduct, determined by fitting each EPR spectrum collected every 5 min after the single oxidation. Interestingly, these time-course variations suggest that the CH_3CH•OH-DMPO adduct continues to be produced in the filtrate after the solution has been separated from the reactive mineral substrate. The origin of this partly delayed production of CH_3CH•OH-DMPO adduct is examined thereafter in the kinetic section.

The production of CH_3CH•OH-DMPO adduct significantly differed among the mineral substrates studied (Figure 1), being ~30% higher for magnetite than for mackinawite, and being negligible for pyrite, similar to the blank. The production of CH_3CH•OH-DMPO adduct appeared more variable for magnetite than for mackinawite over the triplicate experiments (Figure 1). Although yet unexplained, this difference could be due to the ability of nanomagnetite particles to aggregate, which may cause variations in the effective reactive surface among experiments, especially in our high ionic-strength conditions, i.e. 0.525 M phosphate-buffer[25,26].

Another important result could be derived from the EPR monitoring of the magnetite and mackinawite suspensions after 1 min air-oxidation without prior addition of CH_3CH_2OH. Indeed, the results displayed in Figure 1a,b show that no significant signal is detected without CH_3CH_2OH addition, unless a weak CH_3CH•OH-DMPO adduct signal similar in height to that in the blank experiment (Figure 1a,b). This small signal is attributed to the presence of residual CH_3CH_2OH vapor in the glove box atmosphere during our sample preparations. It is especially remarkable that virtually no •OH-DMPO adduct signal is detected without prior addition of CH_3CH_2OH, indicating that •OH radical is not significantly produced after 1 min air-oxidation of magnetite or mackinawite in our 0.525 M phosphate buffered pH 7 conditions. This result indicates that the formation of the CH_3CH•OH-DMPO adduct observed for the CH_3CH_2OH added magnetite or mackinawite suspensions (Figure 1a,b) cannot be due to the reaction of CH_3CH_2OH with •OH radical.

Free-radical production after oxidation of magnetite by H_2O_2 with or without CH_3CH_2OH addition. Unlike the results obtained for air-oxidation, magnetite oxidation by H_2O_2 produced high amounts of the •OH-DMPO adduct in the experiment conducted without added CH_3CH_2OH, as shown in Figure 2. Indeed, the •OH-DMPO adduct signal largely dominated the EPR spectrum, with the following fitting EPR parameters: g_{iso} =2.0054(1), A_{Hiso} = 0.00140(1) cm^{-1} [15.0(1) Gauss], A_{Niso} = 0.00140(1) cm^{-1} [15.0(1) Gauss] with a Gaussian line-shape and a full-width of 1.28(1) Gauss. These parameters are fully consistent with those reported in the literature for this adduct[20,21,27]. A weak signal from the CH_3CH•OH-DMPO adduct was also observed, which is again attributed to the presence of residual CH_3CH_2OH vapor in the glove box atmosphere during our sample preparations. By contrast, oxidation by H_2O_2 of the CH_3CH_2OH added magnetite suspension, produced a strong signal of the CH_3CH•OH-DMPO adduct (Figure 2). These results suggest that oxidation of magnetite by H_2O_2 in our buffered pH 7 conditions lead to •OH radical production. The latter likely quickly reacted with CH_3CH_2OH to form CH_3CH•OH that is then captured by DMPO to form the CH_3CH•OH-DMPO adduct, or was directly captured by DMPO to form the •OH-DMPO adduct in the absence of CH_3CH_2OH[20,27]. It is noticeable that H_2O_2 oxidation generating •OH radicals lead to rapid production of

$CH_3CH•OH$-DMPO or •OH-DMPO adducts, followed by their decay (Figure 2). In contrast, air-oxidation did not involve •OH radicals in our pH 7 experiments, yielded either no significant •OH-DMPO adducts or a build-then-decay of $CH_3CH•OH$-DMPO adduct (Figures 1 and 2), in the absence or presence of added $CH_3CH•OH$, respectively.

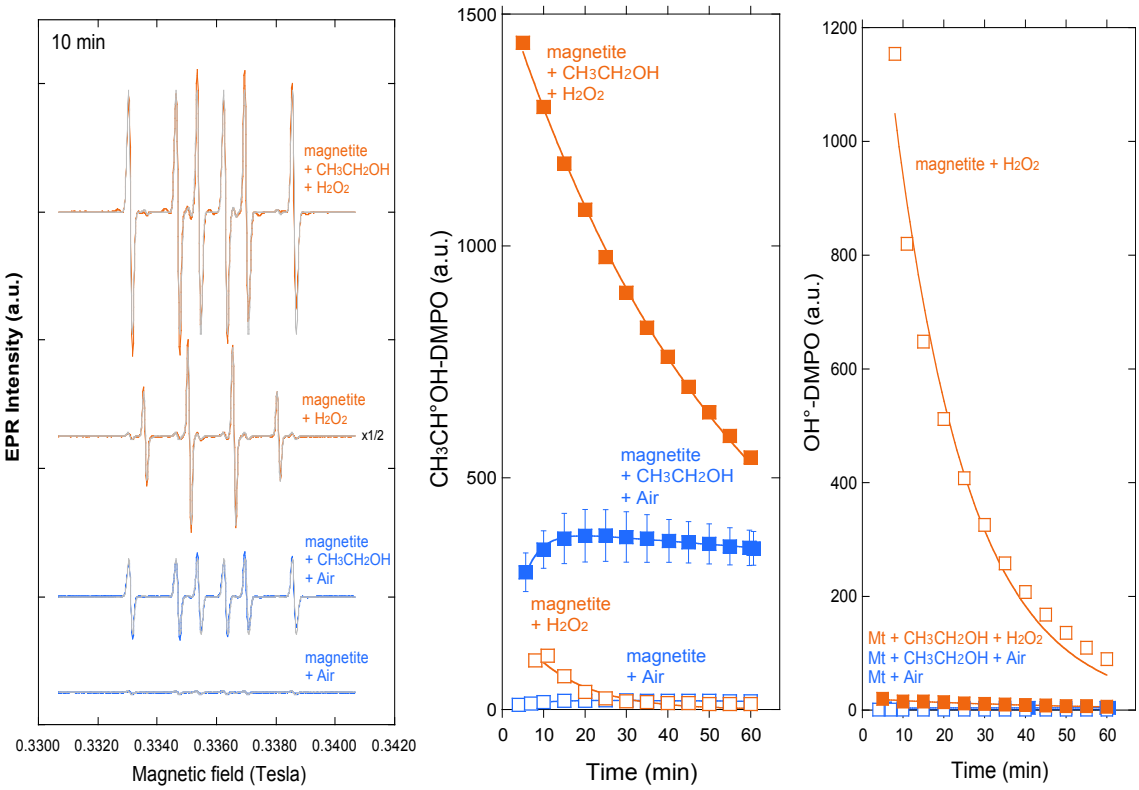

Figure 2. EPR spin trapping analysis of the DMPO-added magnetite suspension (0.525 M phosphate buffer pH 7) filtered after either H_2O_2 addition (orange) or 1 min air bubbling (blue) in the presence or absence of CH_3CH_2OH. Left panel: EPR spectrum of each experiment collected 10 min after having started the 1min air-oxidation. Fitting curves are displayed as light-gray lines, with fitting parameters reported in Table S2. In the absence of ethanol, note the dominant signal of the •OH-DMPO adduct after H_2O_2 addition and the absence of this signal after air-bubbling. Center panel: EPR-monitoring of the $CH_3CH•OH$-DMPO adduct scale-factor from 5 to 60 min after having started the 1 min air-oxidation or H_2O_2 oxidation. Right panel: EPR-monitoring of the •OH-DMPO adduct scale-factor from 5 to 60 min after having started the 1 min air-oxidation or H_2O_2-oxidation (Mt stands for magnetite). The kinetics fitting curves displayed as plain lines are obtained with Eq. 1 or 1', with fitting parameters reported in Table 1.

Effective kinetics of reactive species production. The time-course evolution of the $CH_3CH•OH$-DMPO adduct scale-factor (A) obtained from our EPR monitoring data of air-oxidation (Figure 1) was satisfactorily fitted by a combination of two first-order kinetics model, with A_{max} being the maximum quantity of adduct and, k_{prod} and k_{decay}, the effective production and decay rate constants, respectively (Table 1):

$$A_{\mathrm{CH3CH•OH-DMPO}}(t) = A_{max}\frac{k_{prod}}{(k_{decay}-k_{prod})}\left(e^{-k_{prod}.t} - e^{-k_{decay}.t}\right) \qquad \text{(Eq. 1)}$$

A single first-order decay kinetic model was used to fit the time-course evolution of the •OH-DMPO and $CH_3CH•OH$-DMPO adducts in the H_2O_2-oxidation experiments (Figure 2; Table 1):

$$A_{\bullet\mathrm{OH-DMPO}}(t) = A_{max}e^{-k_{decay}.t} \quad \text{(Eq. 1')}$$

When converting $A_{\max}$ values into molarity unit by comparison with a strong-pitch EPR-standard, the maximum CH_3CH•OH-DMPO adduct concentrations detected in our experiments were found to reach the micro-molar range (Table 1), with about four-fold higher values after H_2O_2-oxidation of magnetite (~ 12.2 µM) than after air-oxidation (~ 3.0 µM).

Table 1. Effective kinetic parameters $A_{\max}$, k_{prod} and k_{decay} obtained by fitting the EPR spectra of the CH_3CH•OH-DMPO and •OH-DMPO adducts as a function of time, according to first-order reaction kinetics (Eqs. 1 and 1'). Corresponding curves are displayed in Figures 1, 2, 3 and 5. The maximum adduct concentration was estimated from the A_{max} value by comparison with a strong-pitch EPR-standard (see Materials and Methods section). All experiments were performed in 0.525 M pH7 phosphate buffer except those labeled by # that were performed in a 0.053 M pH7 phosphate buffer.

CH_3CH•OH-DMPO adduct	***A_{max}*** **(a.u.)**	***k_{prod}*** **(*min^{-1}*)**	***k_{decay}*** **(*min^{-1}*)**	***Chi²***	***R***	$[CH_3CH$•OH-DMPO$]_{max}$ ***(µM)***
magnetite 12mg + CH_3CH_2OH + H_2O_2	1551(9)	*n.a.*	0.0179(2)	1183	0.999	~ 12.21(7)
magnetite 12mg + CH_3CH_2OH + 20 min Air	501(7)	0.133(15)	0.0042(3)	111	0.991	~ 3.95 (5)
magnetite 12mg + CH_3CH_2OH + 1 min Air	389(40)	0.248(70)	0.0019(20)	81	0.992	~ 3.0(4)
magnetite 12mg filtered 0.2 µm + CH_3CH_2OH + 1 min Air	169(3)	0.253(17)	0.0015(5)	98	0.966	~ 1.33(2)
magnetite 12mg filtered 3 kDa + CH_3CH_2OH + 1 min Air	185(2)	0.298(11)	0.0040(3)	27	0.989	~ 1.46(1)
# magnetite 12mg + CH_3CH_2OH + 1 min Air	179(13)	*n.a.*	00012(7)	175	0.990	~ 1.41(10)
mackinawite 4.6mg + CH_3CH_2OH + 20 min Air	409(4)	0.137(15)	0.0046(2)	55	0.996	~ 3.22(3)
mackinawite 4.6mg + CH_3CH_2OH + 1 min Air	300(1)	0.308(4)	0.0045(1)	7	0.999	~ 2.36(1)
mackinawite 4.6mg filtered 0.2 µm + CH_3CH_2OH + 1 min Air	123(3)	0.256(28)	0*	139	0.943	~ 0.97(2)
mackinawite 4.6mg filtered 3 kDa + CH_3CH_2OH + 1 min Air	110(5)	0.237(14)	0*	48	0.979	~ 0.87(4)
# mackinawite 4.6mg + CH_3CH_2OH + 1 min Air	84(1)	0.135(4)	0*	3	0.997	~ 0.66(1)
pyrite 6.2mg + CH3CH2OH + 20 min Air	11(6)	0.05(3)	0*	11	0.782	~ 0.09(1)
pyrite 6.2mg + CH3CH2OH + 1 min Air	10(1)	0.24(8)	0*	6	0.876	~ 0.08(1)
blank + CH_3CH_2OH + 1 min Air	14(1)	0.19(3)	0.006(2)	5	0.856	~ 0.09(1)
magnetite 12mg + H_2O_2	213(28)	*n.a.*	0.074(10)	1092	0.966	~ 1.7(2)
magnetite 12mg + 1 min Air	22(1)	0.144(9)	0.0035(7)	2	0.991	~ 0.17(1)
mackinawite 4.6mg + 1 min Air	20(1)	0.277(18)	0.0146(6)	5	0.999	~ 0.16(1)

•OH-DMPO adduct	***A_{max}*** **(a.u.)**	***k_{prod}*** **(*min^{-1}*)**	***k_{decay}*** **(*min^{-1}*)**	***Chi²***	***R***	$[$•OH-DMPO$]_{max}$ ***(µM)***
magnetite 12mg + CH_3CH_2OH + H_2O_2	21(7)	*n.a.*	0.0210(12)	6	0.986	~ 0.16(1)
magnetite 12mg + CH_3CH_2OH + 1 min Air	4(1)	*n.a.*	*0**	*n.a.*	*n.a.*	~ 0.03(1)
magnetite 12mg + H_2O_2	1622(94)	*n.a.*	0.0545(36)	26196	0.989	~ 12.8(7)
magnetite 12mg + 1 min Air	1(1)	*n.a.*	*0**	2	0.991	~ 0.008(8)

*Note: * fixed value ; n.a.: Eq.1 was not applicable and Eq. 1' was used to fit a single first-order decay.*

Interestingly, the maximum •OH-DMPO adduct concentration (~ 12.2 µM) detected upon H_2O_2-oxidation of magnetite without CH_3CH_2OH addition was similar to the CH_3CH•OH-DMPO adduct concentration (~12.8 µM) detected with CH_3CH_2OH addition (Figure 2; Table 1), which confirmed the ability of CH_3CH_2OH to quench almost the whole •OH pool produced in the presence of H_2O_2[20,27]. In contrast, the maximum concentration of •OH-DMPO adduct (0.01 µM) detected upon air-oxidation of magnetite without CH_3CH_2OH addition was 300-fold lower than the CH_3CH•OH-DMPO adduct concentration detected with CH_3CH_2OH addition (~3.0 µM) (Figure 2; Table 1), which indicated that •OH was not the main reactive species responsible

for CH_3CH_2OH oxidation upon air-oxidation of magnetite. The origin of the CH_3CH•OH-DMPO adduct in this case is further addressed in the next sections.

The effective production rate (k_{prod}) of the CH_3CH•OH-DMPO adduct determined from the rise of this signal after filtration of the solids in the air-oxidation experiments (Figure 1b,d) exhibited comparable values for the three mineral substrates studied as well as for the blank experiment (Table 1), yielding an average value of k_{prod} = 0.25±0.03 min^{-1}, i.e. a half-life of $t_{1/2}$ = 2.8±3 min. (Table 1). This production rate (k_{prod}) is close to the typical oxidation rate of an oxygen saturated ferrous solution at pH 7 (0.16 min^{-1} ; $t_{1/2}$ = 4.3 min[28]. This rise of the CH_3CH•OH-DMPO adduct signal after filtration thus suggested a contribution from dissolved Fe^{2+} species that could further oxidize after filtration, as confirmed by complementary oxidation experiments (Figure 3) and ICP-OES analysis of Fe concentration in the filtrates (Figure 4). Indeed the CH_3CH•OH-DMPO adduct was produced by oxidizing the anoxic filtrates of the magnetite or mackinawite suspensions instead of the full-suspension, which resulted in similar kinetics but lower adduct production (Figure 3; Table 1).

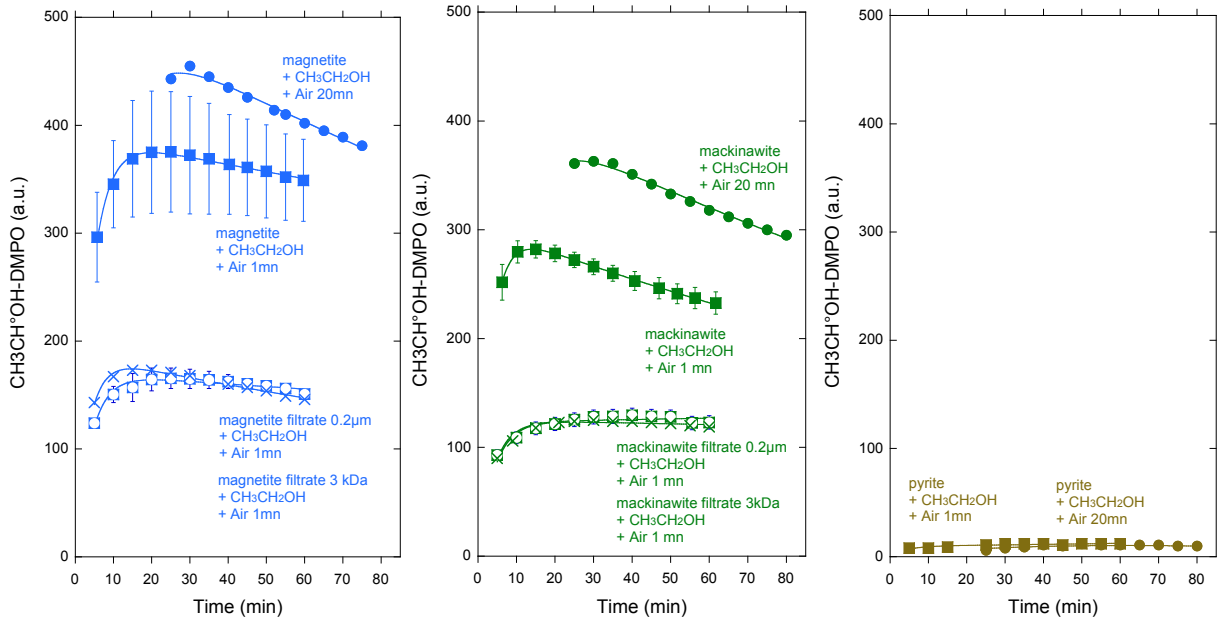

Figure 3 EPR monitoring of the DMPO- and CH_3CH_2OH- added mineral suspensions of magnetite (blue), mackinawite (green), pyrite (brown), after 20 min air bubbling and immediate filtration (plain circles), after 1 min air bubbling, 1 min shaking and immediate filtration (plain squares), and after filtration in anaerobic glove box, 1 min air bubbling, 1 min shaking (0.2 µm : open squares; 3kDa : crosses). The fitting curves displayed as plain lines were obtained with Eq. 1, with fitting parameters reported in Table 1. Experiments conducted in 0.525M phosphate buffer at pH = 7.

For magnetite and mackinawite, respectively, the same amounts of CH_3CH•OH-DMPO adducts were obtained from the 1 min air-oxidation of ultra-filtered (3 kDa) and filtered (0.2 µm) suspensions (Figure 3; Table 1), which was consistent with the similar amount of aqueous Fe detected by ICP-OES in the corresponding filtrates (Figure 4). These similar results obtained using 3 kDa and 0.2µm filters indicated that the contribution of colloidal material to CH_3CH•OH-DMPO adduct production after filtration is negligible in our protocol. Nevertheless, the amount of CH_3CH•OH-DMPO adduct produced by oxidizing the filtrates represented however only ~40% of the amount of adduct produced by oxidizing the full mineral suspension for 1 min (Figure 3; Table 1). This result indicated that Fe(II) from the mineral surfaces (Figure 4; Table S4)

contributed to more than half of the amount of CH_3CH•OH-DMPO adduct produced upon oxidation of the full mineral suspensions (Figure 3; Table1). Partial oxidation of Fe(II) to Fe(III) in the solid phase is also observed directly using XANES spectroscopy upon 1 min air-oxidation of the full mineral suspensions (Figure S4 ; Table S4). The amount of oxidized Fe(II) is however found to be lower than the available amount of surface Fe(II) (Table S4). The remaining available solid Fe(II) pool may then explain the higher CH_3CH•OH-DMPO adduct production observed after 20 min air-oxidation (Figure 3; Table 1).

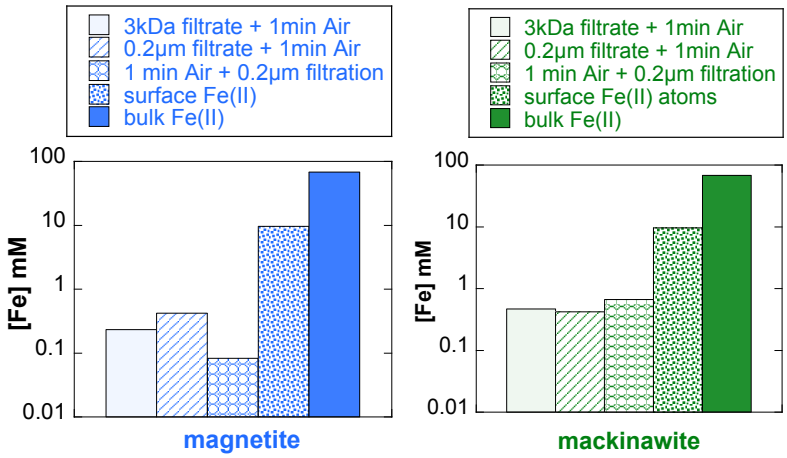

Figure 4. Dissolved and solid iron concentrations in the experiments reported in Figure 3 for magnetite (blue) and mackinawite (green). Reported dissolved concentrations correspond to total iron determined by ICP-OES. Reported solid concentrations correspond to Fe(II) in the added mineral particles (78 mM) split into a surface Fe(II) atoms pool calculated for a surface shell of 3 Å thickness, and a remaining bulk Fe(II) pool, assuming average particle diameters of 140 and 90 Å for our magnetite and mackinawite, respectively (Table S2).

Owing to the long half-life of the CH_3CH•OH-DMPO adduct in our air-oxidation experiments ($t_{1/2}$ = 360 min), we also investigated the production of this adduct by EPR monitoring of the filtrate obtained after 20 min air-oxidation of the mineral suspensions (Figure 3; Table 1). These longer oxidation experiments produced 30–40% more CH_3CH•OH-DMPO adduct than the 1 min air-oxidation experiments and the shape of the kinetic curves approached a simple decay curve (Figure 3), which suggested that the major fraction of both the aqueous and mineral-surface pool of readily oxidizable Fe^{2+} would be likely reached within the 30 min of air-oxidation. The results also confirmed that magnetite was more reactive than mackinawite, and that pyrite was not reactive under our reaction conditions, for a similar equivalent total Fe^{2+}_{solid} concentration (78 mmol.L^{-1}).

Finally, the effective decay rate (k_{decay}) values of the CH_3CH•OH-DMPO adduct were scattered among the various experiments, with half-lives in the 40 – 400 min range. It is noticeable that the decay rate of this adduct in the magnetite oxidation experiments was about 10-fold higher with H_2O_2 addition (k_{decay} = 0.0179 ± 0.0002 min^{-1} ; $t_{1/2}$ = 38 ± 2 min) than without (k_{decay} = 0.0019 ± 0.0002 min^{-1} ; $t_{1/2}$ = 360 ± 40 min) (Table 1), which may be related to the complexity of decay processes for this adduct[29].

Identity of the reactive species produced after air- or H_2O_2-oxidation of magnetite and mackinawite. The results of our air-oxidation experiments in the presence of CH_3CH_2OH indicate that the reaction of

dissolved O_2 with magnetite or mackinawite has produced reactive species able to oxidize CH_3CH_2OH into the hydroxyethyl radical $CH_3CH•OH$. However, the lack of significant hydroxyl radical •OH signal in the air-oxidation experiments conducted in the absence of CH_3CH_2OH shows that •OH is not responsible for CH_3CH_2OH oxidation in our air-oxidation experiments.

The use of CH_3CH_2OH as intermediate radical trap for detecting •OH via the formation of the $CH_3CH•OH$-DMPO adduct is classical, especially to circumvent the ambiguity between genuine •OH-DMPO adduct, i.e. •OH captured by DMPO, from the same adduct deriving from the decomposition of $O_2•^-$-DMPO[20,27]. This latter decomposition is however very limited, typically below a few percent of the $O_2•^-$-DMPO pool[20,30]. However, even though no $O_2•^-$-DMPO adduct signal is observed in our EPR spectra, we cannot exclude the formation of the superoxide radical in our experiments since the half-life of the $O_2•^-$-DMPO adduct is typically shorter (~ 1 min)[30,31] than the delay between the air-oxidation of our mineral suspension and the first EPR spectrum (5 min) of our time-series (Figures 1 and 2). The decay of the $O_2•^-$-DMPO adduct have been reported to be even faster in the presence of Fe^{2+}[30,31], thus requiring more specific spin traps to better stabilize superoxide ion adducts[32,33]. Nevertheless, even if we cannot exclude the formation of $O_2•^-$, this species cannot be responsible for the H-atom abstraction from CH_3CH_2OH observed in our air-oxidation experiments. Indeed, the inability of $O_2•^-$ to directly react with CH_3CH_2OH to form the $CH_3CH•OH$ radical is classically used as for distinguishing it from •OH[20,27].

Another intermediate species has then to be invoked to explain CH_3CH_2OH oxidation in our air-oxidation experiments at pH 7. Such species could be Fe(IV), in the form of the ferryl ion, $Fe^{IV}O^{2+}$, as suggested by several hints. The ferryl ion has been proposed as an additional product of the Fenton reaction, based on experimental[34-40] and theoretical investigations[41-43]. The ferryl ion was especially proposed to explain the decrease in •OH production rate observed in the Fenton reaction when Fe^{2+} is chelated by phosphate, adenosine diphosphate (ADP) and ethylenediaminetetraacetate (EDTA) and to be responsible for oxidizing ethanol when Fe^{2+} is chelated by EDTA[36]. Unlike suggested by Walling and Amarnath[44], the ferryl ion is not considered as an intermediate in the •OH production process, which was rather demonstrated to proceed by direct H_2O_2 homolytic cleavage in the Fenton reaction[45]. However, the ferryl ion could form as an additional species from the reaction of Fe^{2+} with H_2O_2[34-36,39,41,42,44,45] and would be stabilized when iron is chelated by appropriate ligands[35-37,46,47] under near-neutral to alkaline pH conditions[35,36,39,48,49]. More recently, the ferryl ion has been shown to be produced from the reaction of Fe^{2+} with other strong oxidants such as ozone[50-52], peroxysulfates[53,55] and periodate[56].

The formation of the ferryl ion under sole airborne O_2-oxidation of Fe^{2+} is debated, since •OH production is thought to be generated at acidic pH[2,49] and is proposed by some authors for near-neutral pH conditions[3,4,11,12,57,58]. Nevertheless, the ferryl ion has been proposed to form upon air-oxidation of Fe^{2+}[49,59] or zero-valent iron[8,9] at near-neutral pH. The EPR spin trapping studies by Reinke et al.[59] and Welch et al.[60] are particularly relevant to the interpretation of our results. Indeed they show that the $CH_3CH•OH$-DMPO adduct is formed after air-oxidation of dissolved Fe^{2+} in the presence of CH_3CH_2OH, while no •OH-DMPO is detected in the absence of CH_3CH_2OH. Reinke et al.[59] proposed that the ferryl ion may be formed by air-oxidation of Fe^{2+} and would then oxidize CH_3CH_2OH into $CH_3CH•OH$, consistently with the known ability of

the ferryl ion for this hydrogen atom abstraction reaction[8,35,36,50,51]. In addition, Reinke et al.[59] noticed that the intensity of the CH_3CH•OH-DMPO adduct increased with increasing the concentration of phosphate buffer upon homogeneous oxidation of aqueous Fe(II) species, which they explained by the ability of appropriate Fe(II)-ligands to promote Fe(IV) over the hydroxyl radical in the Fenton reaction [35,36,59, 60].

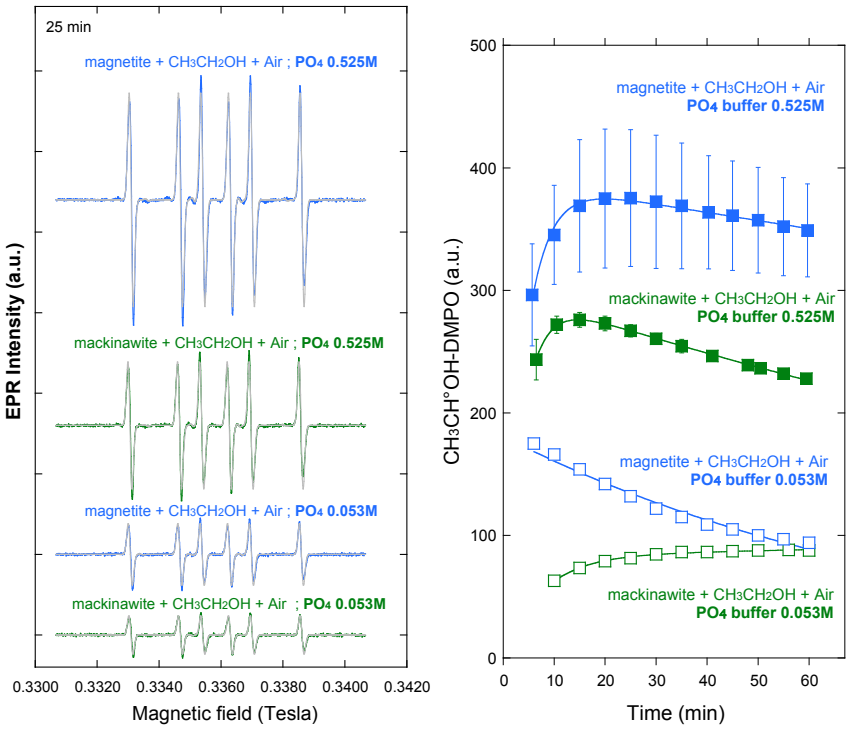

Figure 5. Effect of phosphate concentration (0.053 M or 0.525 M phosphate buffer pH 7) on the EPR spectra for DMPO-added magnetite (blue) or mackinawite (green) suspensions filtered after 1 min air bubbling in the presence of CH_3CH_2OH. Left panel: EPR spectrum of each experiment collected 25 min after having started the 1min air-oxidation. Fitting curves are displayed as light-gray lines, with fitting parameters reported in Table S2. Right panel: EPR-monitoring of the CH_3CH•OH-DMPO adduct scale-factor from 5 to 60 min after having started the 1 min air-oxidation. The kinetics fitting curves displayed as plain lines are obtained with Eq. 1 or 1', with fitting parameters reported in Table 1.

Here, we show that this effect is also observed in the case of heterogeneous air-oxidation of Fe^{2+} from mineral substrates. This result is consistent with a surface-localized oxidant, distinct from the aqueous hydroxyl radical, and recently reported as forming upon oxygenation of mackinawite[10].

Moreover, the results presented in Figure 5 indicate that decreasing the phosphate buffer concentration by a 10-fold factor, from 0.525 M to 0.053 M, decreases the CH_3CH•OH signal by a factor of about 2.5 to 3.5 for magnetite and mackinawite, respectively (Table 1). The mechanisms, by which phosphate and other specific ligands may promote the ferryl ion upon H_2O_2 or air-oxidation of ferrous iron in aqueous media, have not been yet elucidated[35,36,59,60]. Nevertheless, the net boosting of CH_3CHOH oxidation when increasing the concentration of the phosphate buffer supports the formation of the ferryl ion in our experiments.

Based on these findings, and without considering yet the putative role of phosphate, we might hypothesize the following overall reactions for explaining the formation and decay of the observed CH_3CH•OH-DMPO adduct in our air-oxidation experiments of magnetite and mackinawite (Reactions 1a-c to 4):

$Fe^{II}Fe^{III}_2O_{4(magnetite)} + ½\ O_2 + 2H^+ \Leftrightarrow Fe^{IV}O^{2+} + \gamma\text{-}Fe^{III}_2O_{3(maghemite)} + H_2O$ (1a)

$Fe^{II}S_{(mackinawite)} + {}^5/_2\ O_2 \Leftrightarrow Fe^{IV}O^{2+} + SO_4^{2-}$ (1b)

$Fe^{2+} + ½\ O_2 \Leftrightarrow Fe^{IV}O^{2+}$ (1c)

$Fe^{IV}O^{2+} + CH_3CH_2OH \Leftrightarrow Fe^{III}(OH)^{2+} + CH_3CH\bullet OH$; $k = 2.5\ 10^3\ M^{-1}.s^{-1}$[50] (2)

$CH_3CH\bullet OH + DMPO \Leftrightarrow CH_3CH\bullet OH\text{-}DMPO$; $k = 4\ 10^7\ M^{-1}.s^{-1}$[61] (3)

$CH_3CH\bullet OH\text{-}DMPO \Leftrightarrow$ non-paramagnetic species (4)

In reaction 1a, hypothetical production of the ferryl ion is proposed to occur via Fe^{2+} oxidation at the surface of magnetite that is known to transform into maghemite under similar air-oxidation experiments[3] (Figure S4). Reaction 1b represents hypothetical production of the ferryl ion via surface oxidation of FeS, whereas the ultimate solid product was ferrihydrite in our oxidation conditions, as indicated by our EXAFS results (Figure S4). The actual FeS surface oxidation mechanisms may likely be more complex since multiple other reactive species, albeit distinct from aqueous •OH, have been proposed to form, especially surface-localized entity such as high-valent iron or surface-associated hydroxyl or sulfur-based radical[10]. Reaction 1c represents the hypothetical formation of the ferryl ion via air-oxidation of aqueous Fe^{2+}, as proposed in previous studies, though it must be recalled here that Fe^{2+} complexation by appropriate ligands are thought to actually favor the ferryl ion formation upon oxidation[8,59,60].

Once the ferryl ion would have been produced, it would be expected to exert a very fast H-atom abstraction from ethanol[50] (reaction 2), with an effective first-order kinetic constant of ~1000 s^{-1}, i.e. a half-life of 0.7 ms, for the ethanol molarity in our experiments (0.407 M). Since then, the formation of the $CH_3CH\bullet OH$-DMPO adduct[61] (reaction 3) is expected to be even faster with an effective kinetics constant of 1.6 10^6 s^{-1}, i.e. a half-life of 0.4 µs, considering the DMPO molarity in our experiments (0.041 M). Reactions 2 and 3 are thus extremely fast compared to the minute/hour time-scale of our time-course EPR monitoring (Figures 1 and 2), which leads to attribute the observed build and decay of the $CH_3CH\bullet OH$-DMPO adduct signal, to reactions 1a-c and 4, respectively. The observed kinetic constants for the build of the $CH_3CH\bullet OH$-DMPO adduct (Figure 1; Table 1) are close to that of Fe^{2+} air-oxidation at pH = 7, i.e. a half-life of a few minutes, which supports the role of Fe^{2+} air-oxidation in the building of the $CH_3CH\bullet OH$-DMPO adduct signal.

Hypothetical mechanisms for ferryl formation upon aqueous air-oxidation of ferrous iron. According to literature findings discussed above and based on our comparative EPR spin-trapping results obtained with or without CH_3CH_2OH addition, we may hypothesize that $Fe^{IV}O^{2+}$ could form after reaction of dissolved O_2 with the magnetite and mackinawite surface together with aqueous Fe^{2+} species (reactions 1a-c). However, despite this reaction has been proposed previously in the literature[8,59,60], its mechanism is actually unclear for aqueous solution. Indeed, most authors refer to a reaction between Fe^{2+} and H_2O_2 to form $Fe^{IV}O^{2+}$[49,59,60] based on the Fenton reaction mechanisms that intrinsically involve H_2O_2[34-36,39,41,42,44,45].

$Fe^{2+} + H_2O_2 \Leftrightarrow Fe^{IV}O^{2+} + H_2O$ (5)

Reaction 5 is reported to actually compete with the classical Haber-Weiss reaction[31,43,62], the latter, reaction 6, being thought to be rather favored at low pH[2,39,45,48,49,63]:

$$Fe^{2+} + H_2O_2 \Leftrightarrow Fe^{3+} + \bullet OH + OH^- \quad (6)$$

Indeed, in near neutral pH conditions, reaction 5 is thought to proceed via an iron peroxide inner-sphere complex[8,41,42,64], that might convert into an hydroxo ferryl ion, via heterolytic O-O cleavage[39] :

$$Fe^{II}(OH)^+ + H_2O_2 \Leftrightarrow Fe^{II}(OH)(H_2O_2)^+ \Leftrightarrow Fe^{IV}O(OH)^+ + H_2O \quad (5b)$$

In contrast, in acidic conditions, reaction 6 is thought to proceed via a $Fe^{II}(H_2O_2)^{2+}$ complex that might further form the hydroxyl radical via homolytic O-O cleavage[39,45]:

$$Fe^{2+} + H_2O_2 \Leftrightarrow Fe^{II}(H_2O_2)^{2+} \Leftrightarrow Fe^{III}(OH)^{2+} + \bullet OH \quad (6b)$$

In the case of airborne O_2 oxidation of Fe^{2+}, the production of H_2O_2 is actually uncertain but has been proposed to proceed via the superoxide radical[2,3,8,49,57,60]:

$$Fe^{2+} + O_2 \Leftrightarrow Fe^{3+} + O_2\bullet^- \quad (7)$$

which might then react with Fe^{2+}[2,3,8,31,49,65]:

$$Fe^{2+} + O_2\bullet^- + 2H^+ \Leftrightarrow Fe^{3+} + H_2O_2 \quad (8)$$

or might dismutate[2,49,57,60]:

$$2O_2\bullet^- + 2H^+ \Leftrightarrow H_2O_2 + O_2 \quad (9)$$

We cannot exclude initial production of the superoxide radical in our experiments, though we were unable to detect the short living $O_2\bullet^-$-DMPO adduct[30,31] in the present study.

Because phosphate is shown to enhance non-hydroxyl reactive species production in our experiments, one could derive from reaction 5b the following reaction to describe ferryl formation from a ferrous phosphate complex in the presence of phosphate at neutral pH:

$$Fe^{II}(HPO_4) + H_2O_2 \Leftrightarrow Fe^{II}(HPO_4)(H_2O_2) \Leftrightarrow Fe^{IV}O(HPO_4) + H_2O \quad (10)$$

Eventually, based on reactions mechanisms reported for O_2 activation by ligand-stabilized Fe(IV)-species in non-aqueous solvents via μ-peroxo-bridged diiron(III) species[66], one might also hypothesize that Fe^{IV}–phosphate species could directly derive from the O_2-oxidation of Fe^{II}–phosphate species in aqueous systems. Based on the reported O_2-activation pathway[66], one may speculate, for instance, a process as follows at neutral pH:

$$[Fe^{II}(HPO_4)]_2 + O_2 \Leftrightarrow [(HPO_4)Fe^{III}O\text{-}OFe^{III}(HPO_4)] \Leftrightarrow 2[Fe^{IV}O(HPO_4)] \quad (11)$$

Our results (Figures 3 and 4) indicate that both aqueous and surface-bound Fe(II)-phosphate complexes may contribute to putative ferryl formation. Reactions 10 and 11 are yet undemonstrated but might be of interest to investigate for better understanding the formation mechanisms of the ferryl ion in aqueous systems. However, direct detection of Fe(IV) in oxygenated aqueous mineral suspensions would be particularly challenging since only a few occurrence of aqueous Fe(IV) has been directly reported and, yet solely in the presence of strong oxidants as O_3[52, 67-68]. The first study reported the formation of $[Fe^{IV}(O)\text{-}(H_2O)_5]^{2+}$ with a $t_{1/2}$ value of 7s at 25°C from O_3-oxidation or Fe^{2+} at acidic pH[52]. More recent studies using mass-spectroscopy have demonstrated the formation of Fe(IV) from O_3-oxidation of Fe(II)-chloride bulk solution[67] and droplets[68]. Hence, further work will be needed to investigate the actual roles of $O_2^{\bullet-}$, H_2O_2 and of phosphate or other ligands in the putative formation of the ferryl ion during airborne O_2 oxidation of Fe(II)-mineral substrates in aqueous media.

Environmental Implications. Our results show that fine-particle Fe_3O_4 (magnetite) is slightly more efficient than fine-particle FeS (mackinawite) for producing reactive species during a short (1 - 20 min long) air-oxidation in our reaction medium, whereas FeS_2 (pyrite + nanomarcasite) appeared unable to produce similar reactive species within the same amount of time, although with comparable surface areas and similar Fe^{2+} molarity. Although the production of reactive species upon air-oxidation has been scarcely compared for various Fe phases within a same study, it has been reported for specific phases via their ability to convert benzoic acid (BA) into *para*-hydroxybenzoic acid (*p*-HBA)[10,11]. Especially, FeS has been reported to be effective at generating reactive species upon oxygenation[10,11], with the most recent study suggesting that surface reactive species, including hypothetical surface Fe(IV), mainly contribute to BA conversion into to dihydroxybenzoic acid (DHBA) rather than HBA[10].

In this context, our EPR-spin trapping results, are complementary to previously reported findings based on BA-conversion measurements and could then also contribute to help selecting reactive substrates for airborne O_2-based oxidation processes. An EPR-based approach has been for instance recently used to elucidate the radicals involved in HAP photodegradation by Fe-bearing clays[69]. Further work could be envisaged to compare the efficiency of mackinawite and magnetite with that of Fe-bearing clays that have been also recognized as able to produce reactive species[6] and to degrade pollutants[5] upon sole air-oxidation. In contrast, our results suggest that pyrite might not be an efficient candidate for the production of reactive species upon air-oxidation at neutral pH, though it has been proven as an efficient substrate for the heterogeneous Fenton reaction using strong oxidants[70].

Conclusion

Our results show that the hydroxyl radical may not be the major reactive species generated after short air-oxidation (1 - 20 min) of magnetite and mackinawite, which differs with previous results reported using *para*-

hydroxybenzoic acid (*p*-HBA) measurements on mackinawite[11]. This difference may in part arise from the use of a phosphate buffer in our experiments instead of the PIPES buffer used in ref [11]. However, DMPO spin-trapping using ethanol as intermediate radical trap in our EPR experiments performed at high phosphate buffer concentration helps to reveal non-hydroxyl radical species that may actually be present in lower amount in the absence of phosphate. Indeed, a careful analysis by He et al.[10] of the BA conversion products during oxygenation of mackinawite has revealed that a surface species, possibly attributed to Fe(IV), is dominant at pH 7 in HEPES buffer even in the absence of phosphate. Our results on magnetite and mackinawite confirm this latter study in showing that a reactive species distinct from the aqueous hydroxyl radical is produced upon oxygenation of magnetite and mackinawite. It is interpreted as Fe(IV) species since it is favored when increasing phosphate buffer concentration[35,36,59]. This species oxidizes ethanol and produces a strong signal from DMPO-alkyl adducts that is observed with a much lower intensity in the absence of phosphate[4]. Our results also suggest that, in the presence of O_2 instead of strong oxidants, the ferryl ion would be unable to produce •OH, which gives nuance to previous findings from Fenton chemistry[71]. Consequently, we show that ligands such as orthophosphate, that have been proposed to favor the hypothetical formation of the ferryl ion from the oxidation of aqueous Fe^{2+} species[35,36,59,60,72] can dramatically enhance the efficiency of nanocrystalline Fe^{2+}-bearing substrates to produce such a reactive species. This finding raises questions on the putative role that such ligands could have on the identity and proportions of reactive species produced by air-oxidation of natural soils and sediment pore-waters. Further research might then be pursued to actually evaluate the ability of Fe(IV) to degrade organic pollutants upon air-oxidation of Fe^{2+}-bearing substrates, though the role of this species has been recently invoked in organic contaminant degradation processes that use peroxysulfates for oxidizing the iron substrate[54,55].

Supporting Information

Rietveld refinement of XRD powder patterns of the mineral substrates in Figure S1.
Mineralogical composition, unit cell parameters and MCD sizes in Table S1.
Fitting of the CH_3CH•OH-DMPO and •OH-DMPO adducts EPR spectra in Figures S2 and S3.
EPR parameters of the CH_3CH•OH-DMPO adduct in Tables S2 and S3.
Fitting of the Fe *K*-edge XANES and EXAFS spectra for the mineral substrates before and after air-oxidation, in Figure S4.
Dissolved and solid Fe concentrations in air-oxidation experiments in Table S4.

Acknowledgements

The authors thank L. Delbes for his help on XRD platform of IMPMC and F. Skouri and C. Travers for their help in the IMPMC chemistry laboratories. We also thank J. Blanchard and S. Guira for BET surface area measurements at LRS. The SOLEIL synchrotron (Orsay) is acknowledged for having provided beamtime on the SAMBA beamline and the authors are especially indebted to G. Landrot, as well as to A. Zitolo and E. Fonda for the beamline tuning and their help during data collection. This study has been granted by MATISSE labex, ANR DEPOLECO and PIREN Seine research programs.

References

(1) Lee, C. Oxidation of organic contaminants in water by iron-induced oxygen activation: A short review. *Environ. Eng. Res.* **2015**, *20*, 205-211.

(2) Fang, G. D.; Zhou, D. M.; Dionysiou, D. D. Superoxide mediated production of hydroxyl radicals by magnetite nanoparticles: Demonstration in the degradation of 2-chlorobiphenyl. *J. Hazard. Mater.* **2013**, *250*, 68−75.

(3) Ardo, S. G.; Nelieu, S.; Ona-Nguema, G.; Delarue, G; Brest, J.; Elsa, P.; Morin, G. Oxidative Degradation of Nalidixic Acid by Nano-magnetite via Fe^{2+}/O_2-Mediated Reactions. *Environ. Sci. Technol.* **2015,** *49*, 4506-4514.

(4) Cheng, D.; Neumann, A.; Yuan, S.; Liao, W.; Qian, A. Oxidative Degradation of Organic Contaminants by FeS in the Presence of O_2. *Environ. Sci. Technol.* **2020**, *54*, 4091−4101.

(5) Zeng, Q.; Dong, H.; Wang, X.; Yua, T.; Cui, W. Degradation of 1, 4-dioxane by hydroxyl radicals produced from clay minerals. *J. Hazard. Mater.* **2017***, 331*, 88–98.

(6) Yuan, S.; Liu, X.; Liao, W.; Zhang, P.; Wang, X.; Tong, M. Mechanisms of electron transfer from structrual Fe(II) in reduced nontronite to oxygen for production of hydroxyl radicals. *Geochim. Cosmochim. Acta* **2018**, *223*, 422–436.

(7) Joo, S. H.; Feitz, A. J.; Sedlak, D. L.; Waite, T. D. Quantification of the oxidizing capacity of nanoparticulate zero-valent iron. *Environ. Sci. Technol.* **2005**, 39, 1263-1268.

(8) Keenan, C. R.; Sedlak D. L. Factors affecting the yield of oxidants from the reaction of nanoparticulate zero-valent iron and oxygen. *Environ. Sci. Technol.* **2008**, 42, 1262-1267.

(9) Kim, H. H.; Lee, H.; Kim, H-E.; Seo, J.; Hong, S. W.; Lee, J-Y.; Lee C. Polyphosphate-enhanced production of reactive oxidants by nanoparticulate zero-valent iron and ferrous ion in the presence of oxygen: Yield and nature of oxidants. *Water Res.* **2020**, *86*, 66e73.

(10) He, J.; Miller, C. J.; Collins, R.; Wang, D.; Waite, T. D. Production of a surface-localized oxidant during oxygenation of mackinawite (FeS). *Environ. Sci. Technol.* **2020**, *54*, 1167-1176

(11) Cheng, D.; Yuan, S.; Liao, P.; Zhang, P. Oxidizing impact induced by mackinawite (FeS) nanoparticles at oxic conditions due to production of hydroxyl radicals. *Environ. Sci. Technol.* **2016**, *50*, 11646-11653.

(12) Tong, M.; Yuan, S.; Ma, S.; Jin, M.; Liu, D.; Cheng, D.; Liu, X.; Gan, Y.; Wang, Y. Production of abundant hydroxyl radicals from oxygenation of subsurface sediments. *Environ. Sci. Technol.* **2016**, *50*, 214-221

(13) Ona-Nguema, G.; Morin, G.; Wang, Y.; Foster, A.; Juillot, F.; Calas, G.; Brown, Jr. G. E. XANES evidence for rapid arsenic(III) oxidation at magnetite, and ferrihydrite surfaces by dissolved O_2, via Fe^{2+}-mediated reactions. *Environ. Sci. Technol.* **2010***,* 44 (14), 5416-5422.

(14) Noël V.; Marchand, C.; Juillot, F.; Ona-Nguema, G.; Viollier, E.; Marakovic, G.; Olivi, L.; Delbes, L.; Gelebart, F.; Morin, G. EXAFS analysis of iron cycling in mangrove sediments downstream of a lateritized ultramafic watershed (Vavouto Bay, New Caledonia). *Geochim. Cosmochim. Acta* **2014**, *136*, 211-228

(15) Morin G., Noël V., Menguy N., Brest J., Baptiste B., Tharaud M., Ona-Nguema G., Ikogou M., Viollier E., Juillot F. Nickel accelerates pyrite nucleation at ambient temperature. *Geochem. Perspect. Lett.* **2017**, *5*, 6-11.

(16) Baya, C.; Le Pape, P.; Baptiste, B.; Brest, J.; Landrot, G.; Elkaïm, E.; Noël, V.; Blanchard, M.; Ona-Nguema, G.; Juillot, F.; Morin, G. Influence of trace level As or Ni on pyrite formation kinetics at low temperature. *Geochim. Cosmochim. Acta* **2021**, 300, 333-353.

(17) Morin, G.; Bonnin, D. Modeling EPR powder spectra using numerical diagonalization of the spin hamiltonian. *J. Magn. Reson.* **1999**, 136, 176-199.

(18) Ravel, B.; Newville, M.; ATHENA, ARTEMIS, HEPHAESTUS. Data analysis for X-ray absorption spectroscopy using IFEFFIT. *J. Synchrotron Radiat.* **2005**, *12*, 537e541.

(19) Morin, G.; Juillot, F.; Casiot, C.; Bruneel, O.; Personné, J-C.; Elbaz-Poulichet, F.; Leblanc, M.; Ildefonse, Ph.; Calas G. Bacterial formation of tooeleite and mixed arsenic(III) or arsenic(V)-iron(III) gels in the Carnoulès acid mine drainage, France. A XANES, XRD and SEM study. *Environ. Sci. Technol.* **2003**, *37*, 1705-1712.
(20) Finkelstein, E.; Rosen, G. M.; Rauckman, E. J. Production of hydroxyl radical by decomposition of superoxide spin-trapped adducts. *Mol. Pharmacol.* **1982**, *21*, 262-265.
(21) Buettner, G. R. Spin Trapping: ESR parameters of spin adducts. *Free Radic. Biol. Med.* **1987**, 3(4), 259–303.
(22) Kotake, Y.; Kuwata, K.; Janzen, E. G. Electron spin resonance spectra of diastereomeric nitroxyls produced by spin trapping hydroxyalkyl radicals. *J. Phys. Chem.* **1979**, 83, 3024-3028.
(23) Taniguchi, H.; Madden, K. P. DMPO-alkyl radical spin trapping: an in situ radiolysis steady-state ESR study. *Radiat. Res.* **2000**, *153*, 447-453.
(24) Clément, J. L.; Ferré, N.; Siri, D.; Karoui, A.; Rockenbauer, A.; Tordo P. Assignment of the EPR spectrum of 5,5-dimethyl-1-pyrroline N-oxide (DMPO) superoxide spin adduct. *J. Org. Chem.* **2005**, *70*, 1198-1203.
(25) Vikesland, P. J.; Heathcock, A. M.; Rebodos, R. L.; Makus, K. E. Particle size and aggregation effects on magnetite reactivity toward carbon tetrachloride. *Environ. Sci. Technol.* **2007,** *41*, 5277-5283.
(26) Favela-Camacho, S. E.; Samaniego-Benítez, E. J.; Godínez-Garcíac, A.; Avilés-Arellano, L. M.; Pérez-Robles, J. F. How to decrease the agglomeration of magnetite nanoparticles and increase their stability using surface properties. *Colloids Surf. A* **2019**, *574*, 29–35.
(27) Finkelstein, E.; Rosen, G. M.; Rauckman, E. J. Spin trapping of superoxide and hydroxyl radical: Practical aspects. *Arch. Biochem. Biophys.* **1980***, 200(1)*, 1-16.
(28) Singer, P. C.; Stumm, W. Acidic Dine Drainage: the rate-determining step. *Science* **1970**, *167(3921)*, 1121-1123.
(29) Kirino, Y.; Ohkuma, T.; Kwan, T. Spin trapping with 5,5-Dimethylpyrroline-N-oxide in aqueous solution. *Chem. Pharm. Bull.* **1980**, *29*, 29-34.
(30) Buettner, G. R. The spin trapping of superoxide and hydroxyl free radicals with DMPO (5,5-dimethylpyrroline –N-oxide): more about iron. *Free Radic. Res. Commun.* **1993**, *19*, S79-S87.
(31) Buettner, G. R.; Oberley, L. W. Consideration in the spin trapping of superoxide and hydroxyl radical in aqueous systems using 5,5-Dimethyl-1-oxide. *Biochem. Biophys. Res. Commun.* **1978***, 83*, 69-74.
(32) Frejaville, C.; Karoui, H.; Tuccio, B.; Le Moigne, F.; Culcasi, M.; Pietri, S.; Lauricella, R.; Tordo, P. 5-(Diethoxyphosphoryl)-5-methyl-1-pyrroline *N*-oxide: a new efficient phosphorylated nitrone for the in vitro and in vivo spin trapping of oxygen-centered radicals. *J. Med. Chem.* **1995**, *38*, 258-265.
(33) Zhao, H.; Joseph, J.; Zhang, H.; Karoui, H.; Kalyanaraman, B. Synthesis and biochemical applications of a cyclic nitrone spin trap: a relaticely superior trap for detecting superoxide anions and glutathiyl radicals. *Free Radic. Biol. Med.* **2001**, *31*, 599-606.
(34) Bray, W. C.; Gorin M. H. Ferryl ion, a compound of tetravalent iron. *J. Amer. Chem. Soc.* **1932***, 54*, 2124-2125.
(35) Yamazaki, I.; Piette, L. H. ESR spin-trapping studies on the reaction of Fe^{2+} ions with H_2O_2-reactive species in oxygen toxicity in biology. *J. Biol. Chem.* **1990**, *265*, 13589-13594
(36) Yamazaki, I.; Piette, L. H. EPR spin-trapping study on the oxidizing species formed in the reaction of the ferrous ion with hydrogen peroxide. *J. Amer. Chem. Soc.* **1991**, 113, 7588-7593.
(37) Sawyer, D. T.; Kang, C.; Llobet, A.; Redman, C. Fenton reagents (1:1 $Fe^{II}L_x$/HOOH) react via [$L_xFe^{II}OOH(BH+)$] (1) as hydroxylases (RH -> ROH), not as generators of free hydroxyl radicals (HO·). *J. Amer. Chem. Soc.* **1993**, *115*, 5817-5818.
(38) Pignatello, J. J.; Liu, D.; Huston, P. Evidence for an additional oxidant in the photoassisted Fenton reaction. *Environ. Sci. Technol.* **1999**, *33*, 1832-1839.
(39) Bataineh, H.; Pestovsky, O.; Bakac, A. pH-induced mechanistic changeover from hydroxyl radicals to iron(IV) in the Fenton reaction. *Chem. Sci.* **2012**, *3*, 1594.
(40) Lee, H.; Lee, H-J.; Sedlak, D. L., Lee, C. pH-Dependent reactivity of oxidants formed by iron and copper-catalyzed decomposition of hydrogen peroxide. *Chemosphere* **2013**, *92*, 652–658.
(41) Ensing, B.; Buda, F.; Blöch, P.; Baerends, E. J. Chemical involvement of solvent water molecules in elementary steps of the Fenton oxidation reaction. *Angew. Chem. Int. Ed.* **2001**, 40, 2893-895.
(42) Ensing, B.; Buda, F.; Blöch, P.; Baerends, E. J. A Car–Parrinello study of the formation of oxidizing intermediates from Fenton's reagent in aqueous solution. *Phys. Chem. Chem. Phys.* **2002***, 4*, 3619–3627.
(43) Ensing, B.; Buda, F.; Baerends, E. J. Fenton-like chemistry in water: oxidation catalysis by Fe(III) and H_2O_2 *J. Phys. Chem. A* **2003**, *107*, 5722-5731.
(44) Walling, C.; Amrnath, K. Oxidation of Mandelic Acid by Fenton's Reagent. *J. Amer. Chem. Soc.* **1982**, *104*, 1185-1189.

(45) Lloyd, R. V.; Hanna, P. P.; Mason, R. P. (1997) The origin of the hydroxyl radical oxygen in the Fenton reaction. *Free Radic. Biol. Med.* **1997***, 22*, 885-888.

(46) Price, J. C.; Barr, E. W.; Tirupati, B.; Bollinger, J. M.; Krebs, C. The first direct characterization of a high-valent iron intermediate in the reaction of an alpha-ketoglutarate-dependent dioxygenase: a high-spin Fe(IV) complex in taurine/alpha-ketoglutarate dioxygenase (TauD) from Escherichia coli. *Biochemistry* **2003**, 42, 7497-7508.

(47) Lacy, D. C.; Gupta, R.; Kari, L.; Stone, K. L.; Greaves, J.; Ziller, J. W.; Hendrich, M. P.; Borovik, A. S. Formation, Structure, and EPR detection of a High Spin Fe^{IV}-oxo species derived from either an Fe^{III}-oxo or Fe^{III}-OH complex. *J. Amer. Chem. Soc.* **2010**, *132*, 12188-12190.

(48) Halliwell, B.; Gutteridge, J. M. C. (1992) Biologically relevant metal ion-dependent hydroxyl radical generation, an update. *Feder. Eur. Biochem. Soc.* **1992***, 307*, 108-112.

(49) Hug, S.; Leupin, O. Iron-catalyzed oxidation of arsenic(III) by oxygen and by hydrogen peroxide: pH-dependent formation of oxidants in the Fenton reaction. *Environ. Sci. Technol.* **2003***, 37*, 2734-2742.

(50) Jacobsen, F.; Holcman, J.; Sehested, K. Reactions of the ferryl ion with some compounds found in cloud water. *Int. J. Chem. Kinet.* **1998***, 30*, 215-221.

(51) Pestovsky, O.; Bakac, A. Reactivity of aqueous Fe(IV) in hydride and hydrogen atom transfer reactions. *J. Amer. Chem. Soc.* **2004***, 126*, 13757-13764.

(52) Pestovsky, O.; Stoian, S.; Bominaar, E. L.; Shan, X.; Münck, E.; Que, Jr. L.; Bakac, A. Aqueous FeIV=O: spectroscopic identification and oxo-Group exchange. *Angew. Chem. Int. Ed.* **2005**, *44*, 6871-6874.

(53) Dong, H.; Li, Y.; Wang, S.; Liu, W.; Zhou, G.; Xie, Y.; Guan, X. Both Fe(IV) and radicals are active oxidants in the Fe(II)/peroxydisulfate process. *Environ. Sci. Technol. Lett.* **2020***, 7*, 219−224.

(54) Wang, Z.; Jiang, J.; Pang, S.; Zhou, Y.; Guan, C.; Gao, Y.; Li, J.; Yang, Y.; Qiu, W.; Jiang, C. Is sulfate radical really generated from peroxydisulfate activated by Iron(II) for environmental decontamination ? *Environ. Sci. Technol.* **2018**, *52*, 11276−1128.

(55) Wang, Z.; Qiu, W.; Pang, S.; Gao, Y.; Zhou, Y.; Cao, Y.; Jiang, J. Relative contribution of ferryl ion species (Fe(IV)) and sulfate radical formed in nanoscale zero valent iron activated peroxydisulfate and peroxymonosulfate processes. *Water Res.* **2020**, *172*, 115504.

(56) Zong, Y.; Shao, Y.; Zeng, Y.; Shao, B.; Xu, L.; Zhao, Z.; Liu, W.; Wu, D. Enhanced oxidation of organic contaminants by iron(II)-activated periodate: The significance of high-valent iron−oxo species. *Environ. Sci. Technol.* **2021**, *55*, 7634–7642.

(57) Pryor, W.A. Oxy-radicals and related species: Their formation, lifetimes and reactions. *Annu. Rev. Physiol.* **1986**, *48*, 657-667.

(58) Zalma, R.; Bonneau, L.; Guignard, J.; Pezerat, H.; Jaurand, M. C. Formation of oxy radicals by oxygen reduction arising from the surface activity of asbestos. *Can. J. Chem.* **1987**, *65*, 2338-2341.

(59) Reinke, L. A.; Rau, J.; McCay, P. B. Characteristics of an oxidant formed during iron(II) autoxidation. *Free Rad. Biol. Med.* **1994**, *16*, 485-492.

(60) Welch, K. D.; Davis, T. Z.; Aust, S. D. Iron autoxidation and free radical generation: effects of buffers, ligands, and chelators. *Arch. Biochem. Biophys.* **2002**, *397*, 360-369.

(61) Taniguchi, H.; Madden, K. P. An in situ radiolysis time-resolved ESR study of the kinetics of spin trapping by 5,5-dimethyl-1-pyrroline-N-oxide. *J. Am. Chem. Soc.* **1999**, *121*, 11875-11879

(62) Haber, F.; Weiss, J. Über die katalyse des hydroperoxydes. *Naturwissenschaften* **1932**, 20 (51): 948–950.

(63) Halliwell, B.; Gutteridge, J. M. C. Oxygen Free Radicals and Iron in Relation to Biology and Medicine: Some Problems and Concepts. *Arch. Biochem. Biophysics* **1986**, 246, 501-514.

(64) Bossmann, S. H.; Oliveros, E.; Göb, S.; Siegwart, S.; Dahlen, E. P.; Payawan, L.; Straub, M.; Wörner, M.; Braun, A. New evidence against hydroxyl radicals as reactive intermediates in the thermal and photochemically enhanced Fenton reactions. *J. Phys. Chem. A* **1998***, 102*, 55542-5550.

(65) Rush, J. D.: Bielski, B. H. Pulse radiolytic studies of the reactions of HO_2/O_2^- with Fe(II)/Fe(III) ions. The reactivity of HO_2/O_2^- with ferric ions and its implication on the occurrence of the Haber-Weiss reaction. *J. Phys. Chem.* **1985**, *89*, 5062-5066.

(66) Kim, S. O.; Satri, C. V.; Seo, M. S.; Kim, J.; Nam, W. Dioxygen activation and catalytic aerobic oxidation by a mononuclear nonheme Iron(II) Complex. J. Amer. Chem. Soc. **2005**, *127*, 4178-4179.

(67) Gu, A. Y.; Musgrave, C.; Goddard III, W. A.; Hoffmann, M. R.; Colussi, A. J. Role of ferryl ion intermediates in fast Fenton chemistry on aqueous microdroplets. *Environ. Sci. Technol.* **2021**, *55*, 14370–14377.

(68) Enami, S.; Sakamoto, Y.; Colussi, A. J. Fenton chemistry at aqueous interfaces. *Proc. Nat. Acad. Sci. USA* **2014**, *111*, 623-628.

(69) Zhao, X.; Cheng, P.; Borch, T.; Waigi, M. G.; Peng, F.; Gao, Y. Humidity induces the formation of radicals and enhances photodegradation of chlorinated-PAHs on Fe(III)-montmorillonite. *J. Hazard. Mat.* **2022**, 423, 127210.
(70) Liu, Y.; Zhao, Y.; Wang, J. Fenton/Fenton-like processes with in-situ production of hydrogen peroxide/hydroxyl radical for degradation of emerging contaminants: Advances and prospects. *J. Hazard. Mat.* **2021**, *404*, 124191.
(71) Wang, Z.; Qiu, W.; Pang, S.; Guo, Q.; Guan, C.; Jiang, J. Aqueous iron(IV)-oxo complex: an emerging powerful reactive oxidant formed by iron(II)-based advanced oxidation processes for oxidative water treatment. *Environ. Sci. Technol.* **2022**, *56*, 1492−1509.
(72) Wang, Z.; Qiu, W.; Pang, S.; Jiang, J. Effects of chelators on the on the production and nature of the reactive intermediates formed in Fe(II) activated peroxydisulfate and hydrogen peroxide processes. *Water Res.* **2019**, *164*, 114957.

TOC Graphic

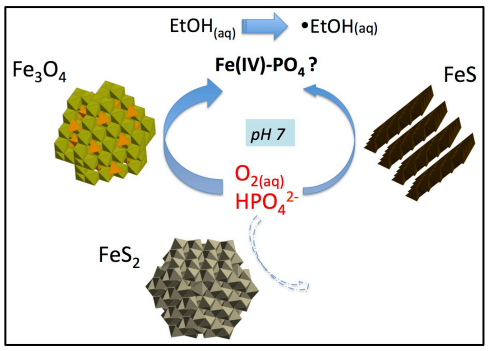

Supporting Information

Phosphate Boosts Nonhydroxyl Radical Species Production upon Air-Oxidation of Magnetite and Iron Sulfides at Neutral pH

Guillaume Morin[1*], Frédéric Averseng[2], Xavier Carrier[2], Pierre Le Pape[1], Yishan Du[1], Yusheng HongE[1], Elora Bourbon[1], Giuseppe Sportelli[2,1], Tiago A. Da Silva[1,2], Alberto Mezzetti[2], Camille Baya[1], Thierry Allard[1], Jessica Brest[1], Maryse Rouelle[3]

[1]Institut de Minéralogie, de Physique des Matériaux et de Cosmochimie (IMPMC)
UMR 7590, CNRS-Sorbonne Université – MNHN – IRD, 4 place Jussieu, 75252 Paris Cedex 05, France

[2]Laboratoire de Réactivité de Surface (LRS)
UMR 7197, Sorbonne Université – CNRS, 4 place Jussieu, 75252 Paris Cedex 05, France

[3]Milieux Environnementaux, Transferts et Interactions dans les hydrosystèmes et les Sols (METIS), UMR 7619, Sorbonne Université – CNRS – EPHE, 4 place Jussieu, 75252 Paris Cedex 05, France

*Corresponding author: guillaume.morin@sorbonne-universite.fr

Content :

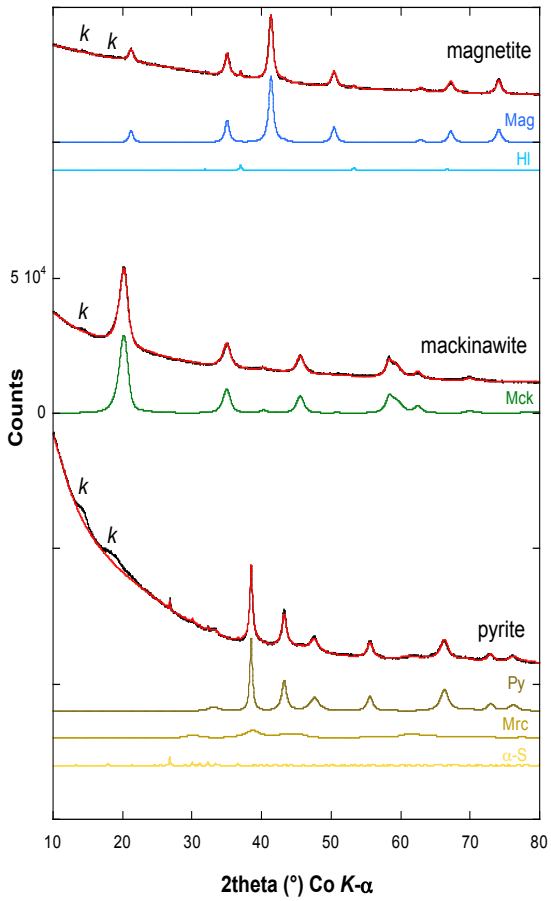

Figure S1. Rietveld refinement of XRD powder patterns of the magnetite, mackinawite and pyrite synthetic substrates prepared and used this study. Refined parameters values are reported in Table S1. Mag : magnetite ; Hl : halite ; Mck : mackinawite ; Py : pyrite ; Mrc : marcasite ; α-S, orthorhombic elemental sulfur; *k* : Kapton® window of the anoxic sample chamber.

Table S1. Mineralogical composition (wt%), unit-cell parameters and mean coherent domain (*MCD*) sizes of the synthetic samples used in this study, as determined by Rietveld analysis of XRD powder patterns displayed in Figure S1. Uncertainties on the last digit are reported under brackets. Rietveld refinement was performed using the XND code[1] with starting parameters taken from crystal structure data by Fleet[2] for magnetite, Wyckoff[3] for halite and pyrite, Lennie et al.[4] for mackinawite, Buerger[5] for marcasite, Rettig and Trotter[6] for α-sulfur. Scale factors were refined for all phases. Unit-cell and line-shape parameters were refined for all phases except halite. Atomic parameters were fixed, except for mackinawite, for which the *z* position of the S atom and the occupancy factor of the Fe atom were refined to 0.221(4) and 106%, respectively.

Sample	***wt%***	***a* (Å)**	***b* (Å)**	***c* (Å)**	***MCD* (001) (nm)**	***MCD* (111) (nm)**	***MCD* (110) (nm)**	***Rwp***
magnetite								0.0141
[a]*magnetite (Fe_3O_4)*	98.6(1)	8.393(9)	8.393(9)	8.393(9)	-	14.5(3)	-	
[b]*halite (NaCl)*	1.4(1)	5.640	5.640	5.640	-	-	-	
mackinawite								0.0156
[c]*mackinawite (FeS)*	100	3.674(12)	3.67(12)	5.048(18)	8.6(8)	-	10.2(6)	
pyrite								0.0206
[d]*pyrite (FeS_2)*	65(2)	5.420	5.420	5.420	18.7(25)	5.4(17)	-	
[e]*marcasite (FeS_2)*	34(2)	4.356	5.414	3.381	-	3.7(9)	-	
[f]*α-sulfur (S_8)*	1.0(4)	10.4646	12.866	24.486	-	-	-	

Note:. - : not measurable

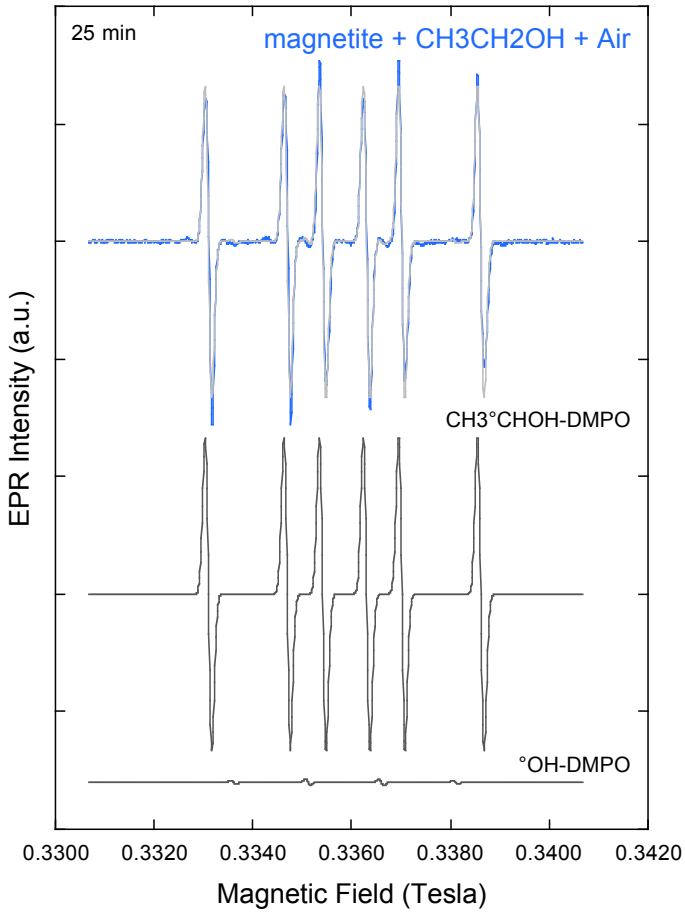

Figure S2. Fitting results for a typical EPR spectrum of the CH_3CH_2OH- and DMPO-added magnetite (12 mg) suspension filtered after air-oxidation. The EPR spectrum (blue line) was collected 25 min after the start of the operation consisting in 1 min air-bubbling, 1 min shaking and immediate filtration. The fitted curve is displayed as light-gray line, and corresponds to 99% of a CH_3CH•OH-DMPO adduct component and 1% of a •OH-DMPO adduct component (Table S2). The asymmetry of the experimental spectrum of the CH_3CH•OH-DMPO adduct is explained by the coexistence of at least two isomers, as shown by a detailed analysis of the more intense spectrum obtained after H_2O_2-oxidation, see Figure S3 and Table S3.

Table S2. EPR parameters of the CH_3CH•OH-DMPO and •OH-DMPO adducts, as determined by fitting the spectrum obtained 25 min after 1 min air-oxidation of magnetite. Uncertainty on the fitting parameters is ±1 on the last digit. See Figure S2.

Adduct	g_{iso}	A_{Hiso} (cm^{-1}) (Gauss)	A_{Niso} (cm^{-1}) (Gauss)	*FWHM* (Gauss)	*%*
Upper curves					
CH_3CH•OH-DMPO	2.0054	0.00217 23.2	0.00150 16.0	1.54	99
•OH-DMPO	2.0054	0.00140 15.0	0.00140 15.0	1.28	1

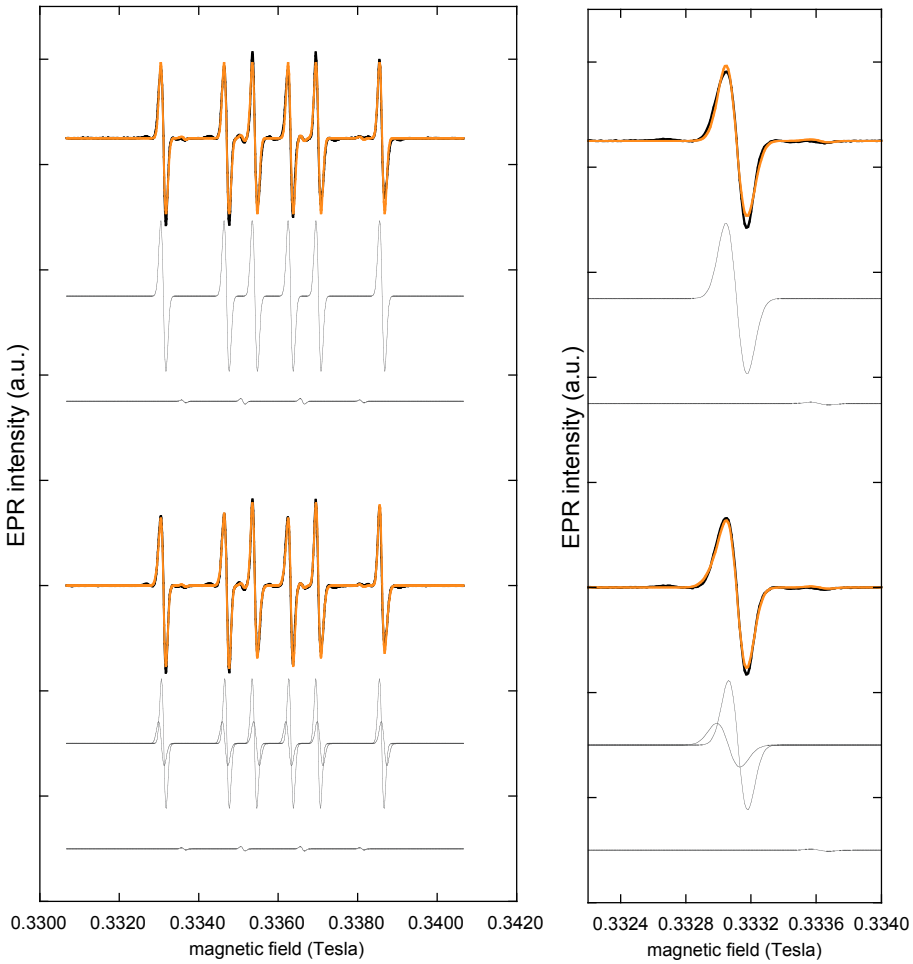

Figure S3. Fitting results for a typical EPR spectrum of the CH_3CH_2OH- and DMPO-added magnetite (12 mg) suspension filtered after H_2O_2-oxidation. The asymmetry of the CH_3CH•OH-DMPO adduct spectrum can be interpreted as a mixture of two isomers spectra (see text). Experimental and fit curves are displayed in black and orange colors, respectively. Weighted fitting components are displayed in light-gray color. Fitting parameters are reported in Table S3.

Table S3. EPR parameters of the CH_3CH•OH-DMPO and •OH-DMPO adducts, as determined by fitting the spectrum obtained 25 min after H_2O_2 oxidation of magnetite. Uncertainty on the fitting parameters is ±1 on the last digit. See Figure S3.

Adduct	g_{iso}	A_{Hiso} (cm^{-1}) (Gauss)	A_{Niso} (cm^{-1}) (Gauss)	*FWHM* (Gauss)	*%*
Upper curves					
CH_3CH•OH-DMPO	2.0054	0.00216 23.1	0.00150 16.0	1.54	99
•OH-DMPO	2.0054	0.00140 15.0	0.00140 15.0	1.28	1
Lower curves					
CH_3CH•OH-DMPO #1	2.0054	0.00214 22.9	0.00150 16.0	1.37	66
CH_3CH•OH-DMPO #2	2.0054	0.00224 23.9	0.00150 16.0	1.68	33
•OH-DMPO	2.0054	0.00140 15.0	0.00140 15.0	1.28	1

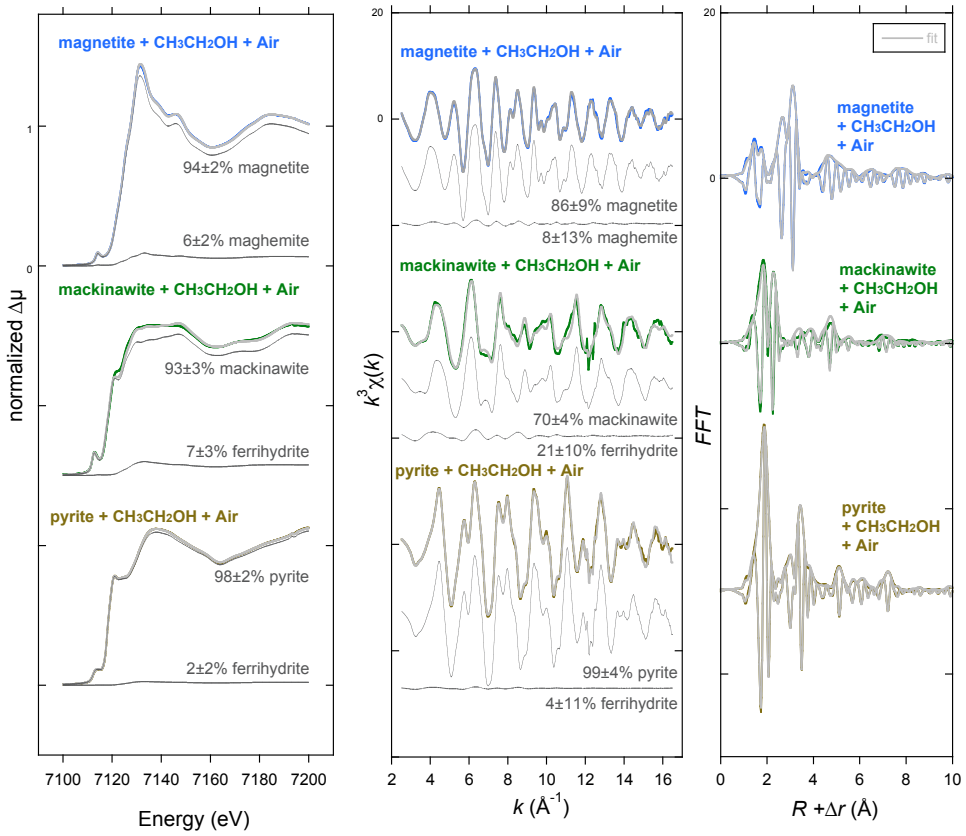

Figure S4. Results of LCF analysis of Fe K-edge XAS data collected on the solid substrate samples before and after 1 min air-bubbling and 1 min shaking of the suspensions added with CH_3CH_2OH, DMPO and a 0.525M phosphate buffer at pH 7. Experimental data for magnetite (12 mg), mackinawite (9.2 mg) and pyrite (6.2 mg) are displayed in blue, green and brown, respectively. Fitted curves are displayed in light-gray color and weighted fitting components are displayed below each spectrum. Left: XANES spectra; Center : k^3-weighted EXAFS spectra ; Right : FFT modulus and imaginary part of the experimental and fitted k^3-EXAFS spectra. The slight mismatch observed in the LCF of oxidized mackinawite could be due to minor contribution from greigite, not included in the fit. XANES LCF results show that our air-oxidation procedure was sufficient to produce detectable change in iron oxidation state in magnetite and mackinawite, likely at the surface of the fine particles. Although less accurate for evaluating iron redox state, EXAFS LCF indicated that maghemite and ferrihydrite were the major oxidation products of magnetite and mackinawite, respectively. Such Fe(II) oxidation is consistent with its possible role in the production of reactive species observed by EPR spin-trapping analysis. In contrast, no significant oxidation of Fe(II) was observed for pyrite, which was found to be unable to produce detectable reactive species in our experimental conditions.

Table S4. Dissolved and solid Fe concentrations in the 1min air-oxidation experiments reported in Figure 3 and 4 and Table 1. Aqueous Fe concentrations were determined by ICP-OES (see Experimental Method). Solid Concentrations correspond to 78 mM Fe(II) added as mineral component, split into surface (3Å thickness) and bulk pools, assuming mean particle sizes of 14 and 9 nm for magnetite and mackinawite, respectively (Table S1). The proportion of oxidized Fe(II) in the solid phase is obtained from XANES LCF analysis results (Figure S4). n.m. : not measured.

Sample	$Fe_{(aq)}^{ICP-OES}$ (mM)	surface $Fe(II)_{(solid)}$ (mM)	bulk $Fe(II)_{(solid)}$ (mM)	Total Fe(II) (mM)	$Fe(II)_{(oxidized\ in\ solid)}^{XANES}$ (mM)
magnetite					
3 kDa filtration + 1 min Air oxidation	0.234	9.6	68.4	78	0
0.2 µm filtration + 1 min Air oxidation	0.422	9.6	68.4	78	0
1 min Air oxidation + 0.2 µm filtration	0.083	9.6	68.4	78	4.7
mackinawite					
3 kDa filtration + 1 min Air oxidation	0.469	14.8	63.4	78	0
0.2 µm filtration + 1 min Air oxidation	0.421	14.8	63.4	78	0
1 min Air oxidation + 0.2 µm filtration	0.667	14.8	63.4	78	5.5
blank	0.001	0	0	0	0

References Cited

(1) Berar, J .F.; Baldinozzi, G. XND code: from X-ray laboratory data to incommensurately modulated phases. Rietveld modeling of complex materials. *Comm. Powder Diffract. Newsletter* **1998**, *20*, 3-5.

(2) Fleet, M. E. The structure of magnetite: symmetry of cubic spinels. J. Solid State Chem. **1986**, *62*, 75-82

(3) Wyckoff, R. W. G. Crystal Structures. Second Edition, Volumes 1–6, **1963**. Interscience, New York.

(4) Lennie, A.R.; Redfern, S. A. T.; Schofield, P. F.; Vaughan, D. J. Synthesis and Rietveld crystal structure refinement of mackinawite, tetragonal FeS. *Mineral. Mag.* **1995**, *59*, 677-683.

(5) Buerger, M. Interatomic distances in marcasite and notes on the bonding in crystals of loellingite, arsenopyrite, and marcasite types. *Zeitsch. Kristallog.* **1937**, *97*, 504-513.

(6) Rettig, S. J.; Trotter, J. Refinement of the structure of orthorhombic sulfur α-S8. *Acta Cryst.* **1987**, *C43*, 2260-2262.